DTU Nanotech
Department of Micro- and Nanotechnology

DTU

Master Thesis, s072160

Theory and Simulation of Electrokinetics in Micro- and Nanochannels

Christoffer P. Nielsen

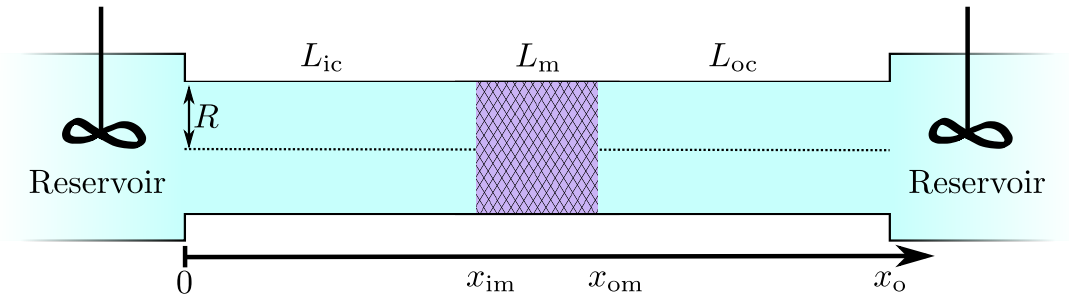

Supervisor: Professor Henrik Bruus
Co-supervisor: Mathias Bækbo Andersen

Department of Micro- and Nanotechnology
Technical University of Denmark

June 29, 2012

Abstract

In this thesis we present results from a numerical study of the effects of surface reactions and bulk reactions on the ion transport across nanoporous ion-selective membranes in microchannels. Transport across such membranes plays an important role for dialysis devices, fuel cells, lab-on-a-chip devices and a number of industrial chemical processes [1, 2, 3, 4].

Although ion-selective membranes have been studied for almost a century proper modelling of their transport properties remains a challenging task. This is both due to the nonlinearity of the governing equations and to the host of mechanisms, which affect the transport. One such mechanism, which has not yet been investigated, is the effect of surface reactions in the microchannels connecting to the membrane.

In the course of the investigations we find that the surface reactions give rise to a varying differential conductance in the so-called overlimiting regime of ion transport through a membrane. We rationalise this and other findings using a combination of analytical results and physical understanding.

Using the developed electrokinetic models we also attempt to simulate the operation of a desalination device with a novel design. No conclusion as to the viability of the design is however arrived at, as the desalination device is found to rely critically on a complicated asymmetric geometry, which cannot be modelled using the employed axisymmetric 3D model.

Dansk resumé

I denne afhandling præsenterer vi resultater fra et numerisk studie af effekterne af kemiske reaktioner på ion-transport igennem nanoporøse ion-selektive membraner i mikrokanaler. Ion-transport på tværs af sådanne membraner spiller en vigtig rolle for dialyse apparater, brændselsceller, lab-on-a-chip systemer og adskillige industrielle kemiske processer [1, 2, 3, 4].

Selvom ion-selektive membraner er blevet studeret i næsten hundrede år er det stadig vanskeligt at modellere deres transportegenskaber ordentligt. Dette skyldes både at de styrende ligninger er stærkt ikke-lineære og at der er en lang række mekanismer som påvirker transporten. En sådan mekanisme, som endnu ikke er blevet undersøgt, er effekten af overfladereaktioner i de mikrokanaler der leder op til membranen.

Vores undersøgelser viser at overfladereaktionerne giver anledning til en varierende differentiel ledningsevne i det såkaldte 'overbegrænsede' regime for ion-transport igennem en ion-selektiv membran. Vi forklarer mekanismerne bag denne og andre effekter vha. analytiske resultater og simple fysiske argumenter.

Vi forsøger endvidere at anvende de udviklede elektrokinetiske modeller til at simulere et afsaltningsapparat med et nyskabende design. Vi når dog ikke frem til nogen konklusion angående designets egnethed, da det bliver klart at afsaltningsapparatet er kritisk afhængigt af en kompliceret asymmetrisk geometri, som ikke kan modelleres vha. den anvendte aksesymmetriske 3D model.

Preface

The present thesis is submitted as fulfilment of the prerequisites for obtaining the Master of Science and Engineering degree at the Technical University of Denmark (DTU). The work has been carried out at the Department of Micro- and Nanotechnology (DTU Nanotech) in the Theoretical Microfluidics Group (TMF) headed by professor Henrik Bruus. The work on this 50 ECTS credits project was carried out from September 2011 to June 2012.

I have several people to thank for help and support during this project. First and foremost, I would like to thank my supervisor Professor Henrik Bruus and my co-supervisor Mathias Bækbo Andersen. The experience and general physical insight of Henrik Bruus as well as Mathias's in-depth understanding of electrokinetic phenomena have been invaluable to the completion of this project.

I am grateful to the entire TMF group for making a great working environment, which allows for both serious study and for cutting loose in a bar or a paintball arena. Also, the wealth of LaTeX and MATLAB knowledge accumulated in the group has been a great help.

Finally, I would like to thank my four roommates Dea, Nils, Niels Ole and Birgitte for lots of support, hot meals and a healthy amount of distraction from the thesis writing.

Christoffer P. Nielsen
Department of Micro- and Nanotechnology
Technical University of Denmark
29 June 2012

Contents

Abstract . . . III
Dansk resumé . . . V
Preface . . . VII
List of Figures . . . X
List of Tables . . . XII
List of Symbols . . . XV

1 Introduction **1**
1.1 Electrokinetics . . . 1
1.2 Ion-selective membranes . . . 2

2 Theory **4**
2.1 Governing equations . . . 4
2.1.1 The continuum hypothesis . . . 4
2.1.2 Fluid dynamical equations . . . 5
2.1.3 Electrostatic equations . . . 6
2.1.4 Transport equations . . . 7
2.1.5 Current density revisited . . . 7
2.2 Chemical reactions . . . 11
2.2.1 Bulk reactions . . . 11
2.2.2 Surface reactions . . . 13

3 Physical Modelling **17**

4 Analytical Modelling **20**
4.1 The diffuse part of the screening layer . . . 20
4.2 Overlimiting current in a microchannel . . . 21
4.3 Dynamic surface charge density . . . 24
4.4 Hydronium distribution . . . 25

5 Numerical Modelling **29**
5.1 The finite element method . . . 29
5.2 Comsol . . . 33
5.3 Mesh Convergence . . . 33

6 An effective 1D model for ion transport **35**
6.1 Modelling of the effective 1D problem 35
6.1.1 1D model of the membrane 38
6.2 Implementation of the 1D model 39
6.3 Results 41
6.3.1 Zero surface charge density 41
6.3.2 Constant surface charge density 41
6.3.3 Dynamic surface charge density 45

7 Axisymmetric 3D model **50**
7.1 Implementation of the 2D model 50
7.2 Results 51

8 A coupled 1D-2D model for the ion transport **54**
8.1 Coupling of 1D and 2D model 54
8.2 Implementation of the coupled 1D-2D model 56
8.3 Results 57

9 Desalination device **60**
9.1 Implementation 61
9.2 Results 62

10 Conclusion and Outlook **66**

List of Figures

1.1 Sketch of dialysis device 2
1.2 Sketch of simple system containing an ion-selective membrane 3

2.1 Hydration of an ionic compound 12
2.2 Sketch of the electric screening layer 15
2.3 Sketch of the potential in the screening layer 15

3.1 Sketch of a system including michrochannels and an ion-selective membrane 18
3.2 Sketch of the model system used in the thesis 19

4.1 Gouy-Chapman solution for the potential in the diffuse layer. 21
4.2 Sketch of auto-dissociation of water close to an ion-selective membrane . . 26
4.3 Influence of the salt ions on the water ions. 27
4.4 Depletion of hydronium in the bulk microchannel. 27

5.1 Sketch of a linearly varying basis function. 30
5.2 Basis function representations of a sine function. 30
5.3 Mesh convergence plot. 34

6.1 Build up of a numerical instability. 40
6.2 I-V curves for model with no surface charge. 42
6.3 Cation concentration and space charge density in a model with no surface charge and no water ions. 42
6.4 Cation concentration and space charge density in a model with no surface charge. 43
6.5 Hydronium concentration and water ion space charge density in a model with no surface charge. 43
6.6 I-V curves for a model with constant surface charge density. 43
6.7 Cation and hydronium concentration profiles for a model with constant surface charge density. 44
6.8 Current plotted versus the surface charge density. 45
6.9 Surface charge density in a microchannel as a function of ionic strength and pH. 46

6.10 I-V characteristics for a model with dynamic surface charge density and $R = 1\,\mu$m. 47
6.11 I-V characteristics for a model with dynamic surface charge density and $R = 5\,\mu$m. 47
6.12 Axial cation concentration in a model with dynamic surface charge and $R = 5\,\mu$m. 48
6.13 Dynamic surface charge density in a model with $R = 5\,\mu$m. 48
6.14 Axial cation concentration for varying inlet concentrations. 49

7.1 Meshing of the 2D domain 51
7.2 I-V curve for 2D model with and without advection. 52
7.3 Cation concentration and velocity field in a 2D model. 53

8.1 Sketch of the model system illustrating which regions are being modelled using a 2D model and which regions are modelled using a 1D model. 56
8.2 I-V curves for a 2D model and a 1D-2D model. 58
8.3 Cation concentration for a 2D model and a 1D-2D model. 58
8.4 Velocity fields for a 2D model and a 1D-2D model. 59
8.5 I-V curve for a 1D-2D model of a channel with dynamic surface charge and $R = 0.6\,\mu$m. 59
8.6 Axial cation concentration for a 1D-2D model of a channel with dynamic surface charge and $R = 0.6\,\mu$m. 59

9.1 Model of a desalination device. 61
9.2 Salt concentration at the side channel outlet for $c_0 = 1\,$mM. 63
9.3 Axial cation concentration in a desalination device for $c_0 = 1\,$mM. 63
9.4 Cation concentration in a desalination device for $c_0 = 1\,$mM. 64
9.5 Magnitude of the current density in a desalination device for $c_0 = 1\,$mM. . 64
9.6 Salt concentration at the side channel outlet for $c_0 = 600\,$mM. 65

List of Tables

2.1 Bare and hydrated radii of some common ions. 12

List of Symbols

Symbol	Description	Unit/value
ρ	Mass density of water	$1 \times 10^3\,\mathrm{kg/m^3}$
$\boldsymbol{u}$	Velocity vector	m/s
u, v	Velocity components	m/s
p	Pressure	Pa
$\boldsymbol{\sigma'}$	Viscous stress tensor	Pa
η	Dynamic viscosity of water	$1 \times 10^{-3}\,\mathrm{Pas}$
ρ_{el}	Space charge density	$\mathrm{C/m^3}$
$\boldsymbol{E}$	Electric field vector	V/m
$\boldsymbol{P}$	Electric polarisation vector	$\mathrm{C/m^2}$
$\boldsymbol{D}$	Electric displacement field	$\mathrm{C/m^2}$
ϕ	Electric potential	V
ϵ_0	Vacuum permittivity	$8.85 \times 10^{-12}\,\mathrm{F/m}$
ϵ_{w}	Permittivity of water	$78\epsilon_0$
ϵ_{m}	Permittivity of a membrane	F/m
σ	Surface charge density	$\mathrm{C/m^2}$
e	Elementary charge	$1.602 \times 10^{-19}\,\mathrm{C}$
c_i	Concentration of chemical species i	$\mathrm{m^{-3}}$
$\boldsymbol{J}_i$	Current density of chemical species i	$\mathrm{m^{-2}s^{-1}}$
R_i	Reaction rate of chemical species i	$\mathrm{m^{-3}s^{-1}}$
D_i	Diffusivity of chemical species i	$\mathrm{m^2/s}$
z_i	Valence of chemical species i	

Symbol	Description	Unit/value
k_B	Boltzmann constant	$1.38 \times 10^{-23}\,\mathrm{J/K}$
T	Temperature	$300\,\mathrm{K}$
$V_\mathrm{T} = \frac{k_\mathrm{B}T}{ze}$	Thermal voltage	$25.7\,\mathrm{mV}$ (for $z = 1$)
μ_i	Electrochemical potential of chemical species i	V
L_i	Generalised mobility of chemical species i	$\mathrm{m^2/Vs}$
F	Helmholtz Free energy	J
U	Internal energy	J
S	Entropy	J/K
a_i	Ionic radius of chemical species i	m
p_0	Water dipole moment	$4.79\,\mathrm{D}$
$c_\mathrm{H}, [\mathrm{H_3O^+}], [\mathrm{H^+}]$	Hydronium concentration	$\mathrm{m^{-3}}$
$c_\mathrm{OH}, \left[\mathrm{OH^-}\right]$	Hydroxide concentration	$\mathrm{m^{-3}}$
K_w	Self-ionization constant of water	$1 \times 10^{-14}\,\mathrm{M^2}$
Γ_i	Surface density of chemical species i	$\mathrm{m^{-2}}$
C_s	Stern capacitance	$2.9\,\mathrm{F/m^2}$
ϵ_P	Porosity of membrane	
τ	Tortuosity of membrane	
N_m	Density of unit charges in membrane	$\mathrm{m^{-3}}$
ρ_m	Space charge density of membrane	$\mathrm{C/m^3}$
ζ, ϕ_d	Potential at the compact layers outer edge	V
λ_D	Debye length	m
L_ic	Length of inlet channel	m
L_m	Length of membrane	m
L_oc	Length of outlet channel	m
R	Radius of microchannel	m
c_0	Salt concentration at reservoir	$\mathrm{m^{-3}}$

Chapter 1

Introduction

The topic of the present thesis *Theory and Simulation of Electrokinetics in Micro- and Nanochannels* is the study of electrokinetic phenomena and in particular the study of microsystems containing nanoporous ion-selective membranes. Below a short introduction to the field of electrokinetics will be given, followed by an introduction to ion-selective membranes.

1.1 Electrokinetics

Consider a particle of positive charge suspended in a liquid. Such a particle may be subjected to a number of different forces. If the particle is small enough Brownian motion will induce it to move randomly about. If the liquid starts to move the particle will be dragged along with the liquid. If an electric field is applied the particle will move under the influence of the Lorentz force, and if there is a nearby wall of negative charge, the particle will move towards the wall. The study of how these forces affect systems containing electrolytes or charged particles is called electrokinetics.

Phenomena relying on electrokinetics are ubiquitous in nature since all living organisms contain large amounts of ionic liquid, and for instance the nervous system is critically dependent on electrokinetics for its function [1]. Electrokinetic phenomena also have a wide array of industrial and technological applications, e.g. in battery technology, lab-on-a-chip devices, chemical sensing, bioanalytics and dialysis [1, 2, 3, 4].

A prominent feature of electrokinetic systems are the so-called screening layers which develop next to surfaces. The screening layers are a response to the surface charge density, which many materials acquire through chemical reactions when submerged in an electrolyte. To screen this surface charge, ions of opposite charge move towards the interface and ions of like charge move away from the interface. Thermal motion of the ions prevent most of them from adsorbing on the surface, and as a result a diffuse screening layer forms next to the surface. These screening layers are important for the ion transport in a system because they, in contrast with the largely charge neutral bulk liquid, can have a quite high space charge density.

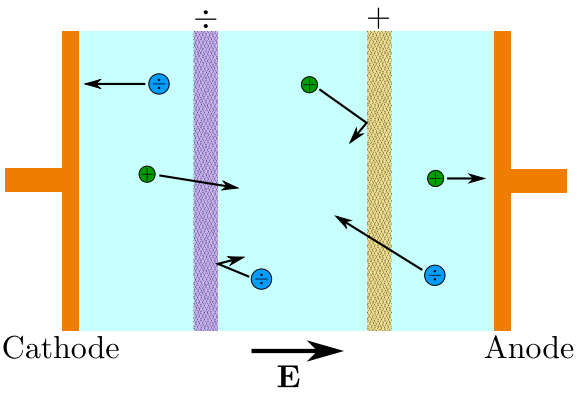

Figure 1.1: *Sketch of the working principle in a dialysis device. An anion and a cation selective membrane are placed between two electrodes. The electric field forces the anions to the right and the cations to the left, and because of the ion-selective membranes the ions are trapped in the middle compartment.*

Modelling electrokinetic phenomena is notoriously difficult due to the disparate length scales set by the system size and the screening layers, and due to the nonlinear coupling of fluid mechanics, diffusion processes, electrodynamics and chemical reactions.

1.2 Ion-selective membranes

Ion-selective membranes are membranes which have a high frozen charge density, causing ions of like charge (coions) to be expelled from the membrane while ions of opposite charge (counterions) can freely pass through the membrane. This peculiar property of ion-selective membranes has found a number of applications, examples of this being dialysis and desalination devices and fuel cells [5]. In figure 1.1 a sketch of a dialysis device is shown. In the middle stream the electrolyte concentration is increased by electrically forcing ions from the edge streams through the ion-selective membranes.

Although the ion transport through an ion-selective membrane is conceptually simple, detailed modelling of it has proven exceedingly difficult. In figure 1.2 a simple system containing a voltage biased cation selective membrane between two reservoirs is shown. Because the anions cannot pass through the membrane they will deplete to the left of the membrane and accumulate to the right. As it is energetically costly to have an unscreened space charge the cation concentration will closely follow that of the anions. Diffusion will act to spread out the concentration profiles and the steady-state profiles will thus resemble the dashed lines seen in figure 1.2.

In the first attempts at modelling ion transport through ion-selective membranes an assumption of exact electroneutrality in the bulk liquid was used [5]. In this model total depletion of both ion species was predicted to the left of the membrane, and as a result the cation current would saturate and approach a limiting current at high voltages.

This theoretical prediction is however not borne out in experiments, where the current is found to increase monotonically with bias voltage and ultimately exceed the limiting

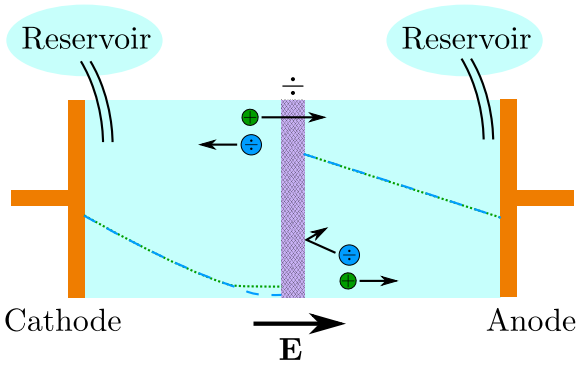

Figure 1.2: *Sketch of a simple system containing a cation-selective membrane. The system is voltage biased and both ends of the system are connected to reservoirs of constant ion concentration. As the anions cannot pass through the membrane they accumulate to the right of the membrane and deplete to the left of the membrane. The resulting concentration profiles are shown in green (cations) and blue (anions).*

current [5]. Part of the reason for this so-called overlimiting current is that an extended space charge region will develop outside the membrane [6]. In this region the cation concentration becomes larger than the anion concentration, and as a consequence the cations can carry a comparatively larger current.

The existence of the extended space charge region does however not fully explain the overlimiting current, and over the years a host of different mechanisms have been suggested to explain it. These mechanisms include water splitting [7], current induced convection and current induced membrane discharge [8].

Recently, it has been found that in microchannels surface conduction through screening layers is an important mechanism for overlimiting current [9]. The reason for this is that, even after the bulk concentration is depleted, a large ion concentration will still be present in the screening layers to screen the wall charge. From this argument it is clear that the magnitude of the surface charge density will be important for the overlimiting current.

To this day, the majority of electrokinetic research is based on an assumption of constant surface charge density. In reality, the surface charge density does however have a complicated dependence on the chemical composition of the surface and of the bulk liquid [10].

In this thesis we will use numerical simulations to improve the understanding of ion transport in microchannels containing nanoporous ion-selective membranes. In these simulations we will include the effects of chemical reactions both in the bulk liquid and at channel walls. Furthermore, we will model a novel design of a desalination device.

Because simulations of electrokinetics can be computationally very demanding we will simplify some of the calculations by developing an effective 1D model for the ion transport.

Chapter 2

Theory

In this chapter the theory applied in the remainder of the report is introduced, and important concepts and their significance are presented.

The chapter starts with a discussion of the continuum hypothesis in which the appropriateness of employing continuum models is considered. The basic continuum equations describing the motion of the liquid, the distribution of the electrical potential and the transport of solvents are then presented. Finally, the modelling of chemical reactions in bulk and at surfaces is treated. This part includes a discussion of the screening layers and introduces the standard model used to describe these.

2.1 Governing equations

2.1.1 The continuum hypothesis

The systems we want to study are mixtures of ions and water which may be subject to external electrical fields. A full description of such systems requires individual modelling of all molecules and their mutual forces, which for typical microscopic system volumes between 10 fL and 1 nL means carrying out simulations involving up to $N \sim 10^{16}$ molecules. Although the computation time of the most efficient molecular dynamics algorithms only scale as $\mathcal{O}(N)$, it is not feasible to perform molecular dynamics simulations of systems with this many particles.

For most applications, knowledge of the detailed behaviour of the constituent molecules may however not be important, because the outcome of any measurement on the system will be an average over a large number of molecules. A theory which only describes the molecular properties on average will thus be sufficient for many purposes. In such a theory the behaviour of the system is described via continuous fields, and the assumption that this gives an adequate description is called 'the continuum hypothesis'.

The justification of the continuum hypothesis can be assessed by considering a so-called fluid particle, which is the domain over which molecules are sampled to give the field value at a given point. To minimise fluctuations in the physical fields such a fluid particle must

be large enough to sample many molecules. On the other hand the fluid particle must be much smaller than the representative physical length scales, so that external forces do not cause the physical properties to vary within the fluid particle. The size of the fluid particle is thus constrained from above and from below. Demanding that the relative deviations due to statistical fluctuations are less than 1 percent, the minimum size of the fluid particle is given as [2]

$$\lambda^* \sim (0.01)^{-2/3} n^{-1/3}, \tag{2.1}$$

where n is the molecular concentration. For water this characteristic length is around 6.7 nm.

The continuum hypothesis starts to break down, when the physically relevant length scales approach this lower bound on the fluid particle size. This may very well be an issue when studying electrokinetic systems, as the characteristic size of the screening layers can be in the sub-nanometer range. In lack of efficient alternatives we will not let that deter us from employing continuum models in the study of elektrokinetic systems, as physically sound albeit inaccurate conclusions may still be extracted from such models. We will thus proceed with developing the continuum theory of electrokinetics, while keeping in mind that caution has to be taken when interpreting results in regions where the continuum hypothesis is invalid.

2.1.2 Fluid dynamical equations

The equations governing the motion of a fluid are continuity equations, expressing the conservation of mass and momentum. The first of these is simply called the continuity equation and reads

$$\partial_t \rho = -\boldsymbol{\nabla} \cdot (\rho \boldsymbol{u}), \tag{2.2}$$

where ρ and $\boldsymbol{u}$ are the density and velocity of the fluid. Liquids are only weakly compressible and for the velocity fields typically encountered in microfluidics they can to a very good approximation be treated as incompressible. The continuity equation thus reduces to

$$\boldsymbol{\nabla} \cdot \boldsymbol{u} = 0. \tag{2.3}$$

The momentum density at a given point in a fluid can change by advection of momentum or by the application of external forces. The momentum conservation equation therefore has the form

$$\partial_t (\rho \boldsymbol{u}) = \boldsymbol{\nabla} \cdot [-\rho \boldsymbol{u}\boldsymbol{u} - p\boldsymbol{I} + \boldsymbol{\sigma}'] + \boldsymbol{f}_{\text{body}}, \tag{2.4}$$

where $\rho \boldsymbol{u}\boldsymbol{u}$ is the advection term, p is the pressure in the fluid, $\boldsymbol{\sigma}'$ is the viscous stress tensor and $\boldsymbol{f}_{\text{body}}$ is a sum of any other body forces which might be present. The viscous stress tensor is given as

$$\boldsymbol{\sigma}' = \eta \left[\boldsymbol{\nabla} \boldsymbol{u} + (\boldsymbol{\nabla} \boldsymbol{u})^T \right] + (\beta - 1)\eta (\boldsymbol{\nabla} \cdot \boldsymbol{u}) \boldsymbol{I}, \tag{2.5}$$

where η is the dynamic viscosity and β is a dimensionless viscosity ratio. Since we are dealing with incompressible fluids the last term in the viscous stress tensor can be neglected.

We will be studying systems with small length scales and low velocities, meaning that the Reynolds number, $Re = \frac{\rho V_0 L_0}{\eta}$, is much smaller than unity. Also, we will only be considering systems in steady-state, so the momentum conservation equation reduces to the steady Stokes equation

$$\boldsymbol{\nabla} \cdot [-p\boldsymbol{I} + \boldsymbol{\sigma}'] + \boldsymbol{f}_{\text{body}} = 0. \tag{2.6}$$

In the systems we will be studying the relevant body forces are gravitational forces and electrostatic forces. The first of these is cancelled by the hydrostatic pressure, leaving only the electrostatic force given as

$$\boldsymbol{f}_{\text{el}} = \rho_{\text{el}} \boldsymbol{E}. \tag{2.7}$$

Here ρ_{el} is the charge density and $\boldsymbol{E}$ is the electrical field.

At channel walls we apply the standard no-slip boundary condition.

2.1.3 Electrostatic equations

The electrostatic part of the problem is governed by Gauss's law

$$\int_{\partial\Omega} \boldsymbol{D} \cdot \boldsymbol{n} \, \mathrm{d}a = Q_{\text{enc}}, \tag{2.8}$$

where $\boldsymbol{D}$ is the electric displacement field, $\boldsymbol{n}$ is a unit normal vector and Q_{enc} is the enclosed free charge. This is the most general statement of Gauss's law and it is valid both for point charges and continuous charge distributions.

We now consider a distribution of point charges spread far apart. Because electrostatic interactions have a very long range, a large number of point charges will contribute to the electric field at any one point. The discrete nature of the electric field sources will therefore be blurred out and the electric field will resemble that of a continuous charge distribution. In this limit we recover the more familiar differential form of Gauss's law

$$\boldsymbol{\nabla} \cdot \boldsymbol{D} = \rho_{\text{el}}, \tag{2.9}$$

which may alternatively be stated in terms of the electrical potential ϕ

$$\boldsymbol{\nabla} \cdot (-\epsilon \boldsymbol{\nabla} \phi) = \rho_{\text{el}}. \tag{2.10}$$

Gauss's law directly gives the boundary condition at a wall as

$$\boldsymbol{n} \cdot \boldsymbol{D} = \sigma, \tag{2.11}$$

where σ is the surface charge density of the wall and $\boldsymbol{n}$ is the walls unit normal vector.

2.1.4 Transport equations

The concentration of a chemical species at a given point can change if there is a net flow towards or away from the point, or if the chemical species is consumed or produced in a chemical reaction. i.e.

$$\partial_t c_i = -\boldsymbol{\nabla} \cdot \boldsymbol{J}_i + R_i, \tag{2.12}$$

where c_i is the concentration of chemical species i, $\boldsymbol{J}_i$ is the current density of that species and R_i is the rate of production by chemical reactions.

The current density has three principal contributions, namely diffusion, electromigration and advection. The diffusive current is given by Fick's law as

$$\boldsymbol{J}_{\text{diff}} = -D_i \boldsymbol{\nabla} c_i, \tag{2.13}$$

where D_i is the diffusivity of chemical species i. The Lorentz force on an ion of charge $z_i e$ in an electric field is given as

$$\boldsymbol{F}_{\text{el},i} = z_i e \boldsymbol{E}. \tag{2.14}$$

Under the influence of this force the ion will quickly reach its terminal velocity, where the driving force is balanced by the Stokes drag. Multiplying the terminal velocity with the particle concentration we find the electromigrative current density as

$$\boldsymbol{J}_{\text{em},i} = c_i \frac{z_i e}{k_{\text{B}} T} D_i \boldsymbol{E}, \tag{2.15}$$

where it has been used that the mobility of the ion is related to its diffusivity through the Einstein relation. The advective current is simply given as the fluid velocity times the ion concentration, so in conclusion the current density of chemical species i becomes

$$\boldsymbol{J}_i = -D_i \boldsymbol{\nabla} c_i + c_i \frac{z_i e}{k_{\text{B}} T} D_i \boldsymbol{E} + c_i \boldsymbol{u}. \tag{2.16}$$

We will be using this form of the current density in the majority of the thesis, and this could well mark the end of the section on governing equations. What follows is a slightly more rigorous derivation of the current density with a few added physical effects, which the reader can skip at his or her discretion.

2.1.5 Current density revisited

In order to derive an expression for the current density $\boldsymbol{J}_i$ we will initially consider the case of a quiescent liquid.

In equilibrium the electrochemical potential μ_i will be the same everywhere in the system and there will be no currents flowing. If we now perturb the system so that it is brought into a non-equilibrium state, currents will spontaneously arise which tend to re-establish equilibrium and equilibrate the electrochemical potential. In general these

currents do not have a simple dependence on the electrochemical potential[1], but for systems close to equilibrium the currents are approximately given as

$$\boldsymbol{J}_i' = -c_i \sum_j L_{ij} \boldsymbol{\nabla} \mu_j. \tag{2.17}$$

The off-diagonal elements in the generalised mobility tensor L_{ij} accounts for interactions between different chemical species, and the prime on $\boldsymbol{J}_i'$ denotes that the fluid velocity has been disregarded. In the following we will use a diagonal mobility tensor and include any interactions between species explicitly in the electrochemical potential.

Adding an advective term to (2.17) an expression for the total current density is obtained

$$\boldsymbol{J}_i = -c_i L_i \boldsymbol{\nabla} \mu_i + c_i \boldsymbol{u}. \tag{2.18}$$

Due to the strong particle-particle interactions of the ionic system it is not possible to derive an exact expression for the electrochemical potential, but under certain assumptions an approximate expression can be found. We first note that given Helmholtz free energy, F, of a system, the electrochemical potential can be found as

$$\mu_i = \frac{\partial F}{\partial N_i}, \tag{2.19}$$

where N_i is the number of particle i. The free energy is given as

$$F = U - TS, \tag{2.20}$$

with U being the internal energy, T the temperature and S the entropy of the system.

A proper calculation of the free energy requires that for all particles the interactions between that particle and every other particle is taken into account. This is clearly not possible to do analytically and instead we will use a so-called mean field approach. In a mean field approach each particle interacts with a mean field instead of interacting with every other particle. This is a huge simplification of the problem and as long as the ion suspension is dilute it can yield quite accurate results. The following analysis is inspired by the approach outlined in [4, 11, 12, 13] and includes a few modifications of our own. To simplify the analysis the case of two oppositely charged ionic species is considered, but the results readily generalise to systems including several ions of different valence.

We will start out by deriving an expression for the internal energy U. The energy is calculated relative to the energy of an initial system which is just pure water. Firstly, we fill the system with a continuous charge distribution increasing the system energy to

$$U_1 = \int_\Omega \int_0^{\rho_{\mathrm{el}}} \phi \, \mathrm{d}\rho_{\mathrm{el}}' \, \mathrm{d}\boldsymbol{r}. \tag{2.21}$$

[1] The reason for this is that the electrochemical potential is only well-defined for en equilibrated system.

We then add one charge q_i at a point, while at the same time removing an amount of the continuous charge distribution around that point, so that the total change in charge is zero. The energy is thereby changed to

$$U_2 = U_1 + q_i\phi - \int_{\Delta\Omega_i} \rho_{\mathrm{el}}\phi \, \mathrm{d}\boldsymbol{r}. \tag{2.22}$$

Continuing this process until the continuous charge distribution is gone we finally get

$$U_3 = U_1 + \sum_i q_i\phi - \sum_i \int_{\Delta\Omega_i} \rho_{\mathrm{el}}\phi \, \mathrm{d}\boldsymbol{r} \tag{2.23a}$$

$$= U_1 + \sum_i q_i\phi - \int_{\Omega} \rho_{\mathrm{el}}\phi \, \mathrm{d}\boldsymbol{r}. \tag{2.23b}$$

Applying Gauss's law to the result and substituting negative and positive ions for the charges we get the internal energy

$$U = \int_\Omega \left(\int_0^{\boldsymbol{D}} \boldsymbol{E}' \cdot \mathrm{d}\boldsymbol{D}' - \boldsymbol{D}\cdot\boldsymbol{E} + ze(c_+ - c_-)\phi \right) \mathrm{d}\boldsymbol{r} \tag{2.24a}$$

$$= \int_\Omega \left(-\int_0^{\boldsymbol{E}} \boldsymbol{D}' \cdot \mathrm{d}\boldsymbol{E}' + ze(c_+ - c_-)\phi \right) \mathrm{d}\boldsymbol{r}. \tag{2.24b}$$

In the above calculation the interaction energy between water molecules and the suspended particles has been disregarded. This is reasonable because each particle will be surrounded by many water molecules regardless of the particles position, and the interaction energy will therefore just give a constant additive contribution to the internal energy. Also, close-range interactions between the particles have not been taken into account. This is not an issue as long as the suspension is dilute, but it will cause the model to break down at high concentrations.

The entropic contribution to the free energy is readily found from the chemical potential of an ideal gas

$$-TS = k_{\mathrm{B}}T \int_\Omega c_+ \ln(a_+^3 c_+) + c_- \ln(a_-^3 c_-) + c_{\mathrm{w}} \ln(a_{\mathrm{w}}^3 c_{\mathrm{w}}) \, \mathrm{d}\boldsymbol{r}. \tag{2.25}$$

Here a_i^3 is the space occupied by one molecule of species i, including any hydration shell the molecule might have. To capture some of the so-called steric effects encountered at high concentrations the entropy of the water molecules have been included in this expression. This prevents the ionic concentrations from exceeding the concentration at close-packing.

The space is occupied by cations, anions and water molecules, so the following relation must hold

$$a_+^3 c_+ + a_-^3 c_- + a_{\mathrm{w}}^3 c_{\mathrm{w}} = 1, \tag{2.26}$$

making c_w expressible in terms of the ion concentrations. The macroscopic polarisation of the medium equals the concentration of water molecules times the average polarisation of a water molecule. i.e.

$$\boldsymbol{P} = c_\mathrm{w} \langle \boldsymbol{p} \rangle . \tag{2.27}$$

The free energy can thus be written as

$$\begin{aligned} F = \int_\Omega & -\frac{1}{2}\epsilon_0 \boldsymbol{E}\cdot\boldsymbol{E} - c_\mathrm{w}\int_0^{\boldsymbol{E}} \langle \boldsymbol{p}\rangle \cdot \mathrm{d}\boldsymbol{E}' + ze(c_+ - c_-)\phi \\ & + k_\mathrm{B}T\left[c_+\ln(a_+^3 c_+) + c_-\ln(a_-^3 c_-) + c_\mathrm{w}\ln(a_\mathrm{w}^3 c_\mathrm{w})\right]\ \mathrm{d}\boldsymbol{r}, \end{aligned} \tag{2.28}$$

and using (2.19) the electrochemical potentials become

$$\mu_\pm = \frac{a_\pm^3}{a_\mathrm{w}^3}\int_0^{\boldsymbol{E}} \langle \boldsymbol{p}\rangle \cdot \mathrm{d}\boldsymbol{E}' \pm ze\phi + k_\mathrm{B}T\left[1 + \ln(a_\pm^3 c_\pm) - \frac{a_\pm^3}{a_\mathrm{w}^3}\left(1+\ln(a_\mathrm{w}^3 c_\mathrm{w})\right)\right]. \tag{2.29}$$

Inserting (2.29) in (2.18) an expression for the current density is obtained

$$\begin{aligned} \boldsymbol{J}_\pm = & -D_\pm\left[\boldsymbol{\nabla}c_\pm + \frac{a_\pm^3}{a_\mathrm{w}^3}c_\pm\frac{a_-^3\boldsymbol{\nabla}c_- + a_+^3\boldsymbol{\nabla}c_+}{1 - a_-^3 c_- - a_+^3 c_+}\right] \\ & + \frac{D_\pm}{V_\mathrm{T}}c_\pm\left[\mp\boldsymbol{\nabla}\phi - \frac{a_\pm^3}{a_\mathrm{w}^3}\frac{\langle\boldsymbol{p}\rangle}{ze}\cdot\boldsymbol{\nabla}\boldsymbol{E}\right] + c_\pm\boldsymbol{u}, \end{aligned} \tag{2.30}$$

where the thermal voltage $V_\mathrm{T} = \frac{k_\mathrm{B}T}{ze}$ has been introduced. The first, third and fifth term in (2.30) are the familiar diffusive, electromigrative and advective current densities. The second term is an added ion diffusion which derives from the diffusion of water molecules. This term becomes important at high ion concentrations and prevents the concentrations from exceeding the concentration at close-packing. The fourth term derives from dielectrophoresis of water which couples to the ions through (2.26). The existence of this dielectrophoretic current density is hitherto unreported in the literature, and it would be interesting to investigate which effect, if any, it has on electrokinetic problems.

From the free energy it should also be possible to derive a requirement on the electrical potential, and such a derivation would provide a nice check of internal consistency in the applied method.

In an isothermal system spontaneous changes can only decrease the free energy

$$\delta F \leq 0, \tag{2.31}$$

implying that the free energy is at a minimum in equilibrium. In equilibrium we thus have

$$\delta F = 0, \tag{2.32}$$

and the corresponding Euler-Lagrange equation for the potential is

$$\frac{\partial F}{\partial \phi} - \sum_i \frac{\partial}{\partial x_i} \left\{ \frac{\partial F}{\partial \frac{\partial \phi}{\partial x_i}} \right\} = 0. \tag{2.33}$$

Inserting the derived expression for the free energy we get

$$\boldsymbol{\nabla} \cdot (\epsilon_0 \boldsymbol{\nabla} \phi + c_{\mathrm{w}} \langle \boldsymbol{p} \rangle) = -ze(c_+ - c_-), \tag{2.34}$$

which, as it should be, is Gauss's law in a dielectric of polarisation $c_{\mathrm{w}} \langle \boldsymbol{p} \rangle$. The applied method thus seems to be internally consistent.

In this thesis we will not make use of this more elaborate electrokinetic model, but merely use it to illustrate that effects other than those included in the simple standard model can be important. As for the dielectrophoretic term in (2.30) it turns out that for most cases it will either be very small or dominated by the steric contribution. One case in which the dielectrophoretic term can be important is when an A/C field is applied. Because the dielectroporetic term depends on the square of the electric field there can be a dielectrophoretic current in the system even though the time average of the field is zero.

2.2 Chemical reactions

2.2.1 Bulk reactions

In the bulk liquid there are two relevant reactions to consider, namely the solvation of salt molecules and the auto-protolysis of water.

Solvation of salt

Solvation, or hydration in the common case where the solvent is water, is the process in which ionic compounds break up and each of the ionic species are stabilised by the solvent molecules. In figure 2.1 this process is sketched for a general diatomic ionic compound AB in water. In reality hydration does of course happen in three dimensions and there will be roughly one water molecule on each of the six sides of the ion.

The hydration reaction can be written as

$$\mathrm{AB}_{(\mathrm{s})} \rightleftharpoons \mathrm{A}^{\mathrm{m}+}_{(\mathrm{aq})} + \mathrm{B}^{\mathrm{m}-}_{(\mathrm{aq})}, \tag{2.35}$$

where m is the magnitude of the ionic charge. For the salts considered in this thesis the equilibrium in (2.35) lies very far to the right, and to simplify the analysis we will therefore assume that the salt is completely dissolved at all times [14].

By forming a hydration shell around the ionic species the water molecules increase the effective radius of the dissolved ions. This is quite important for the kinetics of ions in a solution, as it decreases the mobility and diffusivity below the value which would

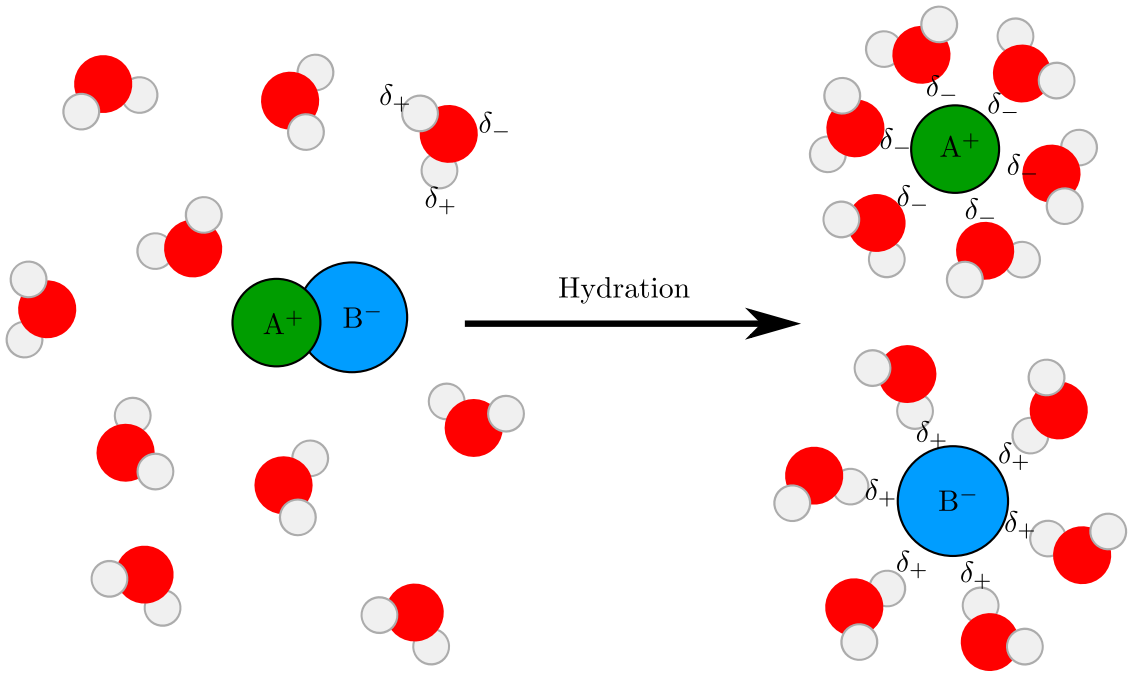

Figure 2.1: *Hydration of a general diatomic ionic compound* AB. *The polarisation of the water molecule is marked by* $\delta_\pm$.

Table 2.1: *Bare and hydrated radii of some common ions [15].*

	Na^+	K^+	Cl^-	Br^-	I^-
Bare radius [nm]	0.117	0.149	0.164	0.180	0.205
Hydrated radius [nm]	0.358	0.331	0.332	0.330	0.331

be expected considering only the bare ionic radius. In table 2.1 is listed the bare and hydrated radii of some common ions. For small ions like sodium the hydration is seen to substantially increase the effective size of the ion.

Auto-protolysis of water

Whereas the details of the hydration reaction (2.35) could be ignored by assuming complete dissolution of the salt, the auto-protolytic reaction of water has to be described in more detail. Pure water reacts with itself to produce hydronium and hydroxide ions according to the reaction

$$2\,H_2O \rightleftharpoons H_3O^+ + OH^-. \tag{2.36}$$

Unless the concentration of solutes becomes very high, the water concentration can be taken to have the constant value $[H_2O] = 55.5\,M$ [14]. Instead of using the equilibrium

constant to describe the reaction (2.36) we can therefore use the self-ionization constant K_w given as

$$K_\mathrm{w} = [\mathrm{H_3O^+}][\mathrm{OH^-}] = K_\mathrm{eq}[\mathrm{H_2O}]^2 \approx 10^{-14}\,\mathrm{M}^2, \tag{2.37}$$

where the last equality is valid at 300 K when the water concentration is 55.5 M. Knowing the concentration of one of the water ions we can thus immediately calculate the concentration of the other.

To treat systems out of equilibrium a more detailed description of the reaction, including the reaction rates, will in general be required. In this work we will however assume local quasi-equilibrium of the chemical reactions, which is physically justified as long as the reactions are much faster than the transport of the reacting chemical species.

In steady-state the transport of water ions is governed by the transport equation (2.12)

$$\boldsymbol{\nabla} \cdot \boldsymbol{J}_\mathrm{OH} = R, \tag{2.38a}$$
$$\boldsymbol{\nabla} \cdot \boldsymbol{J}_\mathrm{H} = R. \tag{2.38b}$$

Here the subscript H is short for the hydronium ion and the reaction rates are identical since the reaction (2.36) produces or consumes one unit of each species. Subtracting (2.38a) from (2.38b) the unknown reaction rate is eliminated and we obtain one equation governing the motion of the water ions

$$\boldsymbol{\nabla} \cdot (\boldsymbol{J}_\mathrm{H} - \boldsymbol{J}_\mathrm{OH}) = \boldsymbol{\nabla} \cdot \boldsymbol{J}_\mathrm{w} = 0, \tag{2.39}$$

where the current density $\boldsymbol{J}_\mathrm{w} \equiv \boldsymbol{J}_\mathrm{H} - \boldsymbol{J}_\mathrm{OH}$ is introduced. Since the concentrations are simply related via the self-ionization constant, equation (2.39) together with appropriate boundary conditions is sufficient to determine the distribution of water ions.

Using the expression (2.16) for the current densities an effective Nernst-Planck equation is obtained from (2.39)

$$\boldsymbol{\nabla} \cdot \left\{ \left(D_\mathrm{H} + D_\mathrm{OH} K_\mathrm{w} c_\mathrm{H}^{-2} \right) \left(\boldsymbol{\nabla} c_\mathrm{H} + c_\mathrm{H} \boldsymbol{\nabla} \phi \right) + \left(K_\mathrm{w} c_\mathrm{H}^{-2} - 1 \right) c_\mathrm{H} \boldsymbol{u} \right\} = 0, \tag{2.40}$$

where c_H is the hydronium concentration.

In the remainder of this thesis cation and anion will be used to denote the positive and negative salt ions while hydronium and hydroxide will be called by their name or collectively referred to as water ions.

2.2.2 Surface reactions

When a solid object is brought into contact with a liquid there will usually be chemical reactions taking place at the surface, which can leave the solid object with a surface charge. In response to this surface charge a screening layer will built up outside the surface, and the structure of this screening layer has been an object of debate for over a century.

Helmholtz was probably the first person to give a mathematical description of the screening layers. In his model the screening layer is viewed as an adsorbed layer of counterions[2], making the combined surface and screening layer effectively act as a capacitor.

The model of Helmholtz makes sense only if the random thermal motion of the ions is disregarded, as this motion will tend to move the adsorbed ions into the liquid phase. This was realised by Gouy, who suggested a rather different model for the screening layers, in which they are modelled as diffuse clouds of ions extending a short distance into the liquid. This model, known as the Gouy-Chapman model[3], is the basis for much electrokinetic research to this day.

A more detailed analysis reveals that there is a limit to how close the hydrated ions can approach the surface. This is both due to their own hydration shell and to an adsorbed monolayer of solvent molecules on the surface. The point of closest approach of the ions set by these constraints is denoted the outer Helmholtz plane (OHP). In contrast the inner Helmholtz plane (IHP) is defined as the locus of any ions adsorbed directly onto the surface. In figure 2.2 is shown a sketch of the particle distribution close to a negatively charged surface.

To model the effect of the finite approach distance, and the existence of adsorbed ions, Stern suggested combining the models of Helmholtz and Gouy, and thus view the screening layer as a compact layer in series with a diffuse layer. The compact layer is characterised by the Stern capacitance C_s, which in lack of good microscopic models of the layer is often found by fitting to experiments. The combined Gouy-Chapman-Stern model is currently the most complete model in common use and the one we shall be employing in this work. In figure 2.3 is shown a sketch of the electrical potential in the screening layer, as it is pictured in the Gouy-Chapman-Stern model. In the region closest to the surface the potential drops linearly from its surface value ϕ_s to the value at the outer Helmholtz plane ϕ_d. In the diffuse layer the potential then drops in an approximately exponential way to its bulk value. Also marked in the sketch is the so-called ζ-potential. The ζ potential is often used in electrohydrodynamics and denotes the value of the potential at the slipping plane. In this work we will assume that the slipping plane corresponds to the outer Helmholtz plane, so that the diffuse potential ϕ_d and the ζ potential are identical.

Having established the approximate structure of the screening layer, we will go on to describe how the solid surface acquires a surface charge in the first place.

In the common case where the solid is either glass or silica, the surface charge mainly derives from dissociation or protonation of silicon hydroxide [23, 10]

$$\mathrm{SiOH} \rightleftharpoons \mathrm{SiO^-} + \mathrm{H^+}, \tag{2.41a}$$
$$\mathrm{SiOH_2^+} \rightleftharpoons \mathrm{SiOH} + \mathrm{H^+}. \tag{2.41b}$$

Assuming that the reactions (2.41) are in equilibrium with equilibrium constants K_SiOH

[2] By counterions is meant ions having the opposite charge of the charged surface.

[3] Chapman was the first to use the model of Gouy to calculate and interpret the differential capacitance of the diffuse layer.

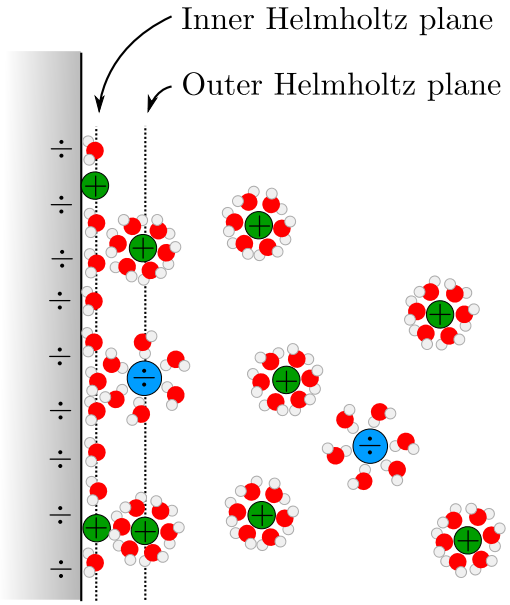

Figure 2.2: *Sketch of the particle distribution close to a negatively charged surface. A monolayer of water molecules is adsorbed on the surface and together with the hydration shell it prevents the ions from moving closer to the surface than the outer Helmholtz plane.*

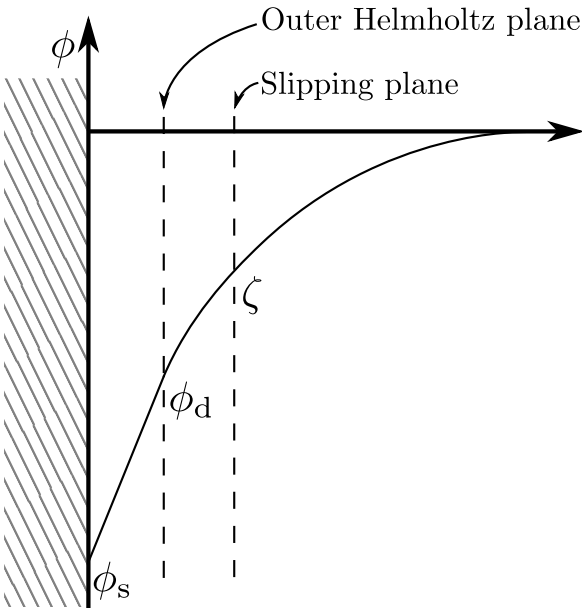

Figure 2.3: *Sketch of the potential in the screening layer next to a negatively charged solid surface. In the innermost region the potential drops linearly over the compact layer of capacitance C_s. In the diffuse layer the potential then drops in an approximately exponential way to its bulk value. The ζ potential denotes the electrical potential at the slipping plane.*

and $K_{\mathrm{SiOH_2^+}}$ respectively, we can write up the mass action laws as

$$\frac{c_{\mathrm{H,s}}\Gamma_{\mathrm{SiO^-}}}{\Gamma_{\mathrm{SiOH}}} = K_{\mathrm{SiOH}}, \tag{2.42a}$$

$$\frac{c_{\mathrm{H,s}}\Gamma_{\mathrm{SiOH}}}{\Gamma_{\mathrm{SiOH_2^+}}} = K_{\mathrm{SiOH_2^+}}. \tag{2.42b}$$

Here Γ_i is the surface density of chemical species i, and the subscript s on the hydronium concentrations denotes that the concentration is evaluated at the surface. From (2.42) the surface charge density is obtained

$$\sigma = e\left(\Gamma_{\mathrm{SiOH_2^+}} - \Gamma_{\mathrm{SiO^-}}\right) = e\Gamma_{\mathrm{SiOH}}\left(\frac{c_{\mathrm{H,s}}}{K_{\mathrm{SiOH_2^+}}} - \frac{K_{\mathrm{SiOH}}}{c_{\mathrm{H,s}}}\right), \tag{2.43}$$

where Γ_{SiOH} can be related to the total surface site density Γ as

$$\Gamma = \Gamma_{\mathrm{SiO^-}} + \Gamma_{\mathrm{SiOH}} + \Gamma_{\mathrm{SiOH_2^+}} \tag{2.44}$$

$$\Leftrightarrow \Gamma_{\mathrm{SiOH}} = \Gamma \left(1 + \frac{c_{\mathrm{H,s}}}{K_{\mathrm{SiOH_2^+}}} + \frac{K_{\mathrm{SiOH}}}{c_{\mathrm{H,s}}} \right)^{-1}. \tag{2.45}$$

Assuming that the hydronium is Boltzmann distributed in the compact layer, the hydronium concentration at the surface $c_{\mathrm{H,s}}$ can be related to the concentration at the outer Helmholtz plane $c_{\mathrm{H,d}}$

$$c_{\mathrm{H,s}} = c_{\mathrm{H,d}} e^{-\frac{\sigma}{V_{\mathrm{T}} C_{\mathrm{s}}}}, \tag{2.46}$$

where $\frac{\sigma}{C_{\mathrm{s}}}$ is the potential drop over the compact layer and $V_{\mathrm{T}} \equiv \frac{k_{\mathrm{B}} T}{ze}$ is the thermal voltage. The hydronium concentration at the outer Helmholtz plane $c_{\mathrm{H,d}}$ does in turn depend on the potential drop over the diffuse layer, implying that the electrostatic boundary condition (2.11) becomes highly non-linear.

Chapter 3

Physical Modelling

In this thesis we study systems consisting of microchannels connected to nanoporous ion-selective membranes. Such systems can be realised in a number of different ways, an illustrative example being a system constructed in the group of Martin Bazant at MIT. A sketch of their system is shown in figure 3.1. Rather than laboriously fabricating a large number of microchannels a layer of tiny glass beads is placed in the system, and the so-called glass frit this creates is full of irregularly shaped microchannels of approximate radius $R \sim 0.6\,\mu$m. The nanoporous membrane is made of nafion which is a chemically very stable anionic polymer. The membrane will thus be selective towards cations and in contrast to the membranes studied in [8] its properties will be largely independent of the chemical environment. As a simple model of this and similar systems we will use a negatively charged membrane situated between two cylindrical glass or silica microchannels connected to well-mixed reservoirs as shown in figure 3.2.

Here we have used simple reservoir boundary conditions at the microchannel terminals rather than electrodes. We do this to simplify the problem, and because the primary goal of this thesis is to study the microchannel-membrane interface and not the effects of electrode reactions on the interface. Using reservoir boundary conditions is only physically justified as long as the concentration fields are smooth and slowly varying near the reservoir. To ensure that this is the case microchannels of a considerable length are used where possible.

Nafion acquires its negative charge by ionization of sulfonic acid groups [16, 17]

$$\mathrm{RSO_3H} \rightleftharpoons \mathrm{RSO_3^-} + \mathrm{H^+}. \tag{3.1}$$

Since sulfonic acid is a quite strong acid it can be taken to ionize completely in water. In most nafion membranes the concentration of sulfonic acid groups available for ionization is around 2 M [18, 19], and we can thus take the charge density of the membrane to be $\rho_\mathrm{m} = -e2\,\mathrm{M}$.

The detailed structure of nafion membranes has been a topic of much research, but so far no conclusive model has emerged [16, 17]. The analysis of the nafion structure is greatly complicated by the fact that it swells and rearranges when hydrated. The structure influences the transport in the membrane, since the distance a particle has to travel is effectively increased in a very tortuous material. The effects of the detailed

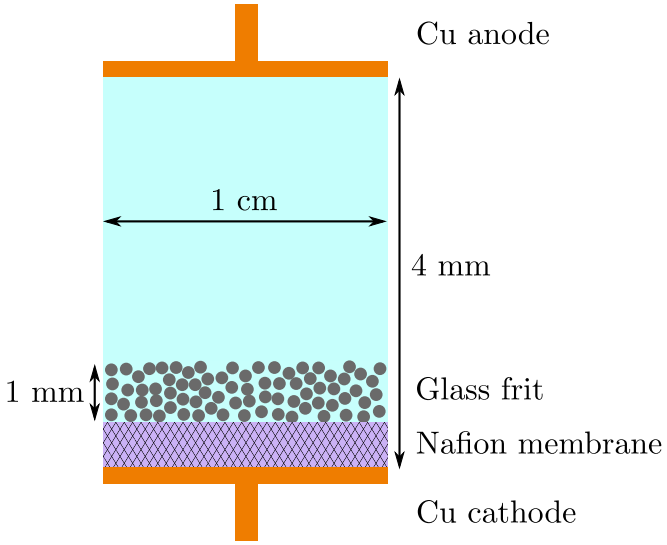

Figure 3.1: *Sketch (not to scale) of a system including microchannels and an ion-selective membrane constructed in the group of Martin Bazant. The pore size of the glass frit roughly corresponds to a radius of* $0.6\,\mu$m.

nafion structure are not part of this study, so we will let the membrane porosity be fixed at the typical membrane value $\epsilon_P = 0.4$ [20] and estimate the tortuosity from the simple expression [21]

$$\tau = \frac{(2-\epsilon_P)^2}{\epsilon_P}. \tag{3.2}$$

As the structure will primarily affect the very low voltage drop inside the membrane, the results obtained using these estimates are expected to be of reasonable generality. From [22] the dielectric constant of dry nafion is given as $\epsilon_{\text{nafion}} \approx 3.5$. Assuming that a linear combination of the dielectric constants of nafion and water gives a good estimate of the dielectric constant of the hydrated membrane, we then have $\epsilon_m = \epsilon_P\epsilon_w + (1-\epsilon_P)\epsilon_{\text{nafion}} \approx 33$.

Because of the nanometer pore size of the nafion membrane we expect the fluid velocity to nearly vanish inside the membrane. We will therefore assume that advection has a negligible influence in the membrane, and for the microchannel flow we will use a no slip boundary condition on the membrane surface.

For the reactions on the surface of the glass/silica microchannels we use the equilibrium constants [23] $K_{\text{SiOH}} = 10^{-6.8}$M and $K_{\text{SiOH}_2^+} = 10^{1.9}$M. The total surface site density is set to [24] $\Gamma = 8\,\text{nm}^{-2}$ and we use the value $C_s = 2.9\,\text{F/m}^2$ for the Stern capacitance [23].

We investigate the case where the dissolved salt is sodium chloride, so the salt ion diffusivities are given as $D_+ = D_{\text{Na}^+} = 1.33 \times 10^{-9}\,\text{m}^2/\text{s}$ and $D_- = D_{\text{Cl}^-} = 2.08 \times 10^{-9}\,\text{m}^2/\text{s}$ [25]. The diffusivities of the water ions are also given in [25] as $D_{\text{H}} = 9.31 \times 10^{-9}\,\text{m}^2/\text{s}$, $D_{\text{OH}} = 5.30 \times 10^{-9}\,\text{m}^2/\text{s}$.

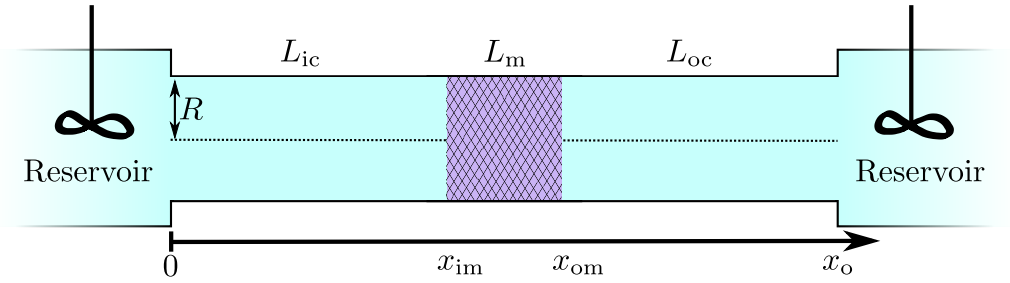

Figure 3.2: *The model system used in this thesis. Two well-mixed reservoirs are connected via a microchannel with a nafion membrane in the middle.*

Chapter 4

Analytical Modelling

To aid our physical understanding of electrokinetic systems some simple analytical results are presented in this chapter.

4.1 The diffuse part of the screening layer

We consider a simple system consisting of an infinite translationally invariant plane of surface charge density σ next to a liquid with two dissolved ionic species $c_\pm$ of opposite charge $\pm ze$. In equilibrium the behaviour of the diffuse part of the screening layer can be found from the field equations derived in chapter 2.

Requiring that the current densities (2.16) vanish we obtain

$$\boldsymbol{J}_\pm = -D_\pm \boldsymbol{\nabla} c_\pm \mp c_\pm \frac{ze}{k_\mathrm{B}T} D_\pm \boldsymbol{\nabla}\phi = 0 \tag{4.1}$$

$$\Rightarrow c_\pm = c_0 e^{\mp \phi/V_\mathrm{T}}, \tag{4.2}$$

where c_0 is the concentration far away from the wall where the potential is zero. For future convenience a normalised potential $\tilde{\phi} \equiv \phi/V_\mathrm{T}$ is defined.

Inserting the concentrations in Gauss's law (2.9) we arrive at the Poisson-Boltzmann equation

$$\boldsymbol{\nabla}\cdot(-\epsilon\boldsymbol{\nabla}\phi) = -2zec_0 \sinh\left(\tilde{\phi}\right). \tag{4.3}$$

Assuming that the permittivity has a constant value equal to that of pure water ϵ_w the above equation can be rewritten

$$\nabla^2\tilde{\phi} = \frac{1}{\lambda_\mathrm{D}^2}\sinh\left(\tilde{\phi}\right), \tag{4.4}$$

where the Debye length is defined as

$$\lambda_\mathrm{D} \equiv \sqrt{\frac{\epsilon_\mathrm{w} V_\mathrm{T}}{2zec_0}}. \tag{4.5}$$

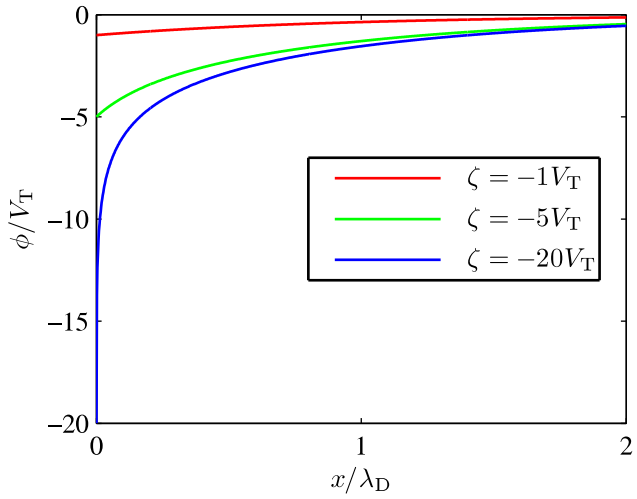

Figure 4.1: *The potential in the diffuse part of the screening layer obtained from the Gouy-Chapman solution. For large ζ potentials the characteristic length of the diffuse layer is seen to be significantly smaller than the Debye length.*

For monovalent ions in a typical concentration of 1 mM the Debye length is around 10 nm.

In the limit of low potentials (the Debye-Hückel limit) equation (4.4) can be linearised, and the Debye length is seen to be a characteristic size of the screening layer. For larger potentials the characteristic size of the screening layer can however be significantly smaller than the Debye length.

In the effectively one dimensional problem of an infinite plane, equation (4.4) is integrable and has the Gouy-Chapman solution

$$\phi = 4V_\mathrm{T} \tanh^{-1}\left[\tanh\left(\frac{\zeta}{4V_\mathrm{T}}\right) e^{-\frac{x}{\lambda_\mathrm{D}}}\right], \tag{4.6}$$

where x is the distance from the plane. The potential ζ at the outer Helmholtz plane can be related to the surface charge density through the Grahame relation[1]

$$\sigma = 2V_\mathrm{T}\frac{\epsilon_\mathrm{w}}{\lambda_\mathrm{D}} \sinh\left(\frac{\zeta}{2V_\mathrm{T}}\right). \tag{4.7}$$

In figure 4.1 the potential in the diffuse layer is plotted for different values of the ζ potential. For large potentials the characteristic length of the diffuse layer is seen to be much smaller than the Debye length.

4.2 Overlimiting current in a microchannel

In narrow microchannels with nanoporous ion-selective membranes a reasonably accurate expression for the overlimiting current can be found analytically.

[1]The Grahame relation is found by integrating (4.4) once.

What normally complicates the analysis of overlimiting current is the extended space charge region, which develops in front of the ion-selective membrane. In the case at hand the majority of the charge in a cross-section of the microchannel will however stem from the screening layers, and it is thus a decent approximation to neglect the space charge region and assume electroneutrality in the bulk liquid. In the case of two ionic species $c_\pm$ of opposite charge $\pm ze$ the cross-sectional averages of the concentrations will therefore be related as

$$ze\left(\langle c_+\rangle - \langle c_-\rangle\right) + 2\frac{\sigma}{R} = 0, \tag{4.8}$$

for a cylindrical microchannel of radius R.

Because the microchannel is narrow advection will only give a negligible contribution to the current densities, and the average current densities become

$$\langle J_+\rangle = -D_+\partial_x\langle c_+\rangle - D_+\langle c_+\rangle\partial_x\tilde{\phi}, \tag{4.9a}$$

$$\langle J_-\rangle = -D_-\partial_x\langle c_-\rangle + D_-\langle c_-\rangle\partial_x\tilde{\phi} = 0. \tag{4.9b}$$

The last equality is valid in steady-state, where the cation selective membrane prevents an anion current from running in the system. Equation (4.9b) is easily integrated to give $\langle c_-\rangle = c_0 e^{\tilde{\phi}-\tilde{V}_0}$, where c_0 is the inlet concentration and $\tilde{V}_0$ is the normalised inlet voltage.

Using (4.8) the result can be inserted in (4.9a) to give

$$\langle J_+\rangle = -D_+\partial_x\left(c_0 e^{\tilde{\phi}-\tilde{V}_0} - 2\tfrac{\sigma}{zeR}\right) - D_+\left(c_0 e^{\tilde{\phi}-\tilde{V}_0} - 2\tfrac{\sigma}{zeR}\right)\partial_x\tilde{\phi}. \tag{4.10}$$

Assuming constant or slowly varying surface charge density and using that the average current density is constant the above equation can be integrated once

$$\frac{\langle J_+\rangle}{D_+}x = 2c_0\left(1 - e^{\tilde{\phi}-\tilde{V}_0}\right) + 2\frac{\sigma}{zeR}(\tilde{\phi}-\tilde{V}_0). \tag{4.11}$$

At the membrane ($x = L_{\mathrm{ic}}$) the potential is $\tilde{V}_1$ so the current-voltage characteristic becomes

$$\frac{\langle J_+\rangle}{D_+}L_{\mathrm{ic}} = 2c_0\left(1 - e^{\tilde{V}_1-\tilde{V}_0}\right) + 2\frac{\sigma}{zeR}(\tilde{V}_1-\tilde{V}_0). \tag{4.12}$$

The first term on the left hand side saturates above a few thermal voltages and is responsible for the classical limiting current. The second term gives a constant differential conductance in the overlimiting regime.

The above analysis is due to Dydek *et al.* [9].

Because the potential $\tilde{V}_1$ in front of the membrane is a dependent variable, it is impractical to let it be a parameter in the solution (4.12). We will therefore extend the above analysis to include the potential drop over the membrane.

In the membrane screening layers the diffusive and electromigrative currents are in opposite directions and very large compared to the total current. The particle distribution

within the screening layers can thus to good approximation be found by simply balancing the diffusive and electromigrative currents. i.e. the concentrations just outside the membrane can be related to the concentration just inside the membrane via a Boltzmann factor. Assuming charge neutrality in the membrane, the change in potential $\Delta\tilde{V}$ from outside to inside the membrane can therefore be found by solving

$$\epsilon_{\mathrm{P}} ze \left(c'_{+} e^{-\Delta\tilde{V}} - c'_{-} e^{\Delta\tilde{V}} \right) - eN_{\mathrm{m}} = 0, \tag{4.13}$$

where $c'_{\pm}$ are the concentrations just outside the membrane, ϵ_{P} is the membrane porosity and N_{m} is the density of negative charges in the membrane. In a perfectly selective membrane the anion concentration vanishes inside the membrane and we find the potential change as

$$\Delta\tilde{V} = -\ln\left(\frac{N_{\mathrm{m}}}{c'_{+} z\epsilon_{\mathrm{P}}}\right). \tag{4.14}$$

Inside the membrane the cation concentration is constant $c_{+,\mathrm{m}} = \frac{N_{\mathrm{m}}}{z\epsilon_{\mathrm{P}}}$ and due to electroneutrality the electric field is also constant $E_{\mathrm{m}} = -\frac{\Delta\tilde{V}_{\mathrm{m}}}{L_{\mathrm{m}}}$. The cation current in the membrane is therefore

$$J_{+} = -f_{\mathrm{r}} D_{+} \frac{N_{\mathrm{m}}}{z\epsilon_{\mathrm{P}}} \frac{\Delta\tilde{V}_{\mathrm{m}}}{L_{\mathrm{m}}}, \tag{4.15}$$

where $f_{\mathrm{r}} = \epsilon_{\mathrm{P}}/\tau$ is a hindrance factor which accounts for the effects of porosity and tortuosity on the ion transport. The potential change from one end of the membrane to the other is then

$$\Delta\tilde{V}_{\mathrm{m}} = -\frac{J_{+}}{D_{+}} \tau L_m \frac{z}{N_{\mathrm{m}}} \tag{4.16}$$

On the right hand side of the membrane the expression relating voltage and current (4.12) takes the form

$$\frac{\langle J_{+} \rangle}{D_{+}} (x - x_{\mathrm{o}}) = 2c_0 \left(1 - e^{\tilde{\phi}}\right) + 2\frac{\sigma}{zeR}\tilde{\phi}, \tag{4.17}$$

where c_0 is the concentration of the outlet reservoir which is at zero potential. Just to the right of the membrane the potential is $\tilde{V}_2$ and the above expression gives

$$\frac{\langle J_{+} \rangle}{D_{+}} (-L_{\mathrm{oc}}) = 2c_0 \left(1 - e^{\tilde{V}_2}\right) + 2\frac{\sigma}{zeR}\tilde{V}_2. \tag{4.18}$$

The total change in potential over the system can be written

$$V_0 = (V_1 - V_0) + \Delta V_1 + \Delta V_{\mathrm{m}} - \Delta V_2 + (0 - V_2), \tag{4.19}$$

where $\Delta V_{1,2}$ are the potential changes over the left and right membrane interfaces respectively.
The equations (4.12) and (4.18) can be solved for the potentials and after some math a current-voltage relationship is obtained from (4.19)

$$\begin{aligned}\tilde{V_0} =& I_+ R_{\mathrm{res}}(L_{\mathrm{ic}} + L_{\mathrm{oc}}) + I_+ R_{\mathrm{res,m}} L_{\mathrm{m}} + \ln\left[\frac{2 + \mathrm{W}\left(2\delta \exp\left(2\delta + I_+ R_{\mathrm{res}} L_{\mathrm{oc}}\right)\right)}{2 + \mathrm{W}\left(2\delta \exp\left(2\delta - I_+ R_{\mathrm{res}} L_{\mathrm{ic}}\right)\right)}\right] \\ &+ \mathrm{W}\left(2\delta \exp\left(2\delta - I_+ L_{\mathrm{ic}} R_{\mathrm{res}}\right)\right) - \mathrm{W}\left(2\delta \exp\left(2\delta + I_+ L_{\mathrm{oc}} R_{\mathrm{res}}\right)\right), \end{aligned} \tag{4.20}$$

where $\delta \equiv -\frac{c_0 z e R}{2\sigma}$ is the inlet number of ions in the bulk divided by the number of ions in the screening layer. $R_{\mathrm{res}} \equiv -\frac{1}{D_+ 2\pi R \sigma}$ is the ohmic resistance of the cations in the screening layer and $R_{\mathrm{res,m}} \equiv \frac{\tau}{D_+ e \pi R^2 N_{\mathrm{m}}}$ is the ohmic resistance of the cations in the membrane.

The Lambert W function solves $\mathrm{W}(x)e^{\mathrm{W}(x)} = x$, and for positive arguments it is a monotonously increasing sublinear function.

The first and second terms in (4.20) are the ohmic voltage drops over the screening layers and the membrane respectively. The third term is the voltage drop over the two membrane interfaces and the fourth and fifth terms are the voltage drops over the bulk of the microchannels.

In section 6.3.2 this current voltage relationship is plotted and compared to results from a more elaborate numerical model.

4.3 Dynamic surface charge density

As seen above, the magnitude of the surface charge density is the key determinant of the overlimiting current in a microchannel. To get a feel for how the surface charge density depends on the physical parameters we will derive an approximate expression for it. In this derivation only the reaction (2.41a) is taken into account, as it will dominate for most realistic parameter values. Furthermore, it is used that only a small fraction of the surface sites react so that Γ_{SiOH} is well approximated by Γ. The surface charge density is then approximately given as

$$\sigma = -\frac{e\Gamma K_{\mathrm{SiOH}}}{c_{\mathrm{H,s}}}. \tag{4.21}$$

In equilibrium the hydronium concentration in the screening layer is Boltzmann distributed, so the concentration at the surface can be written as

$$c_{\mathrm{H,s}} = c_{\mathrm{H,bulk}} \exp\left(-\tilde{\zeta} - \frac{\sigma}{V_{\mathrm{T}} C_{\mathrm{s}}}\right). \tag{4.22}$$

From the Grahame relation (4.7) we have

$$e^{-\tilde{\zeta}} = \exp\left(-2\sinh^{-1}\left(\frac{\lambda_{\mathrm{D}}\sigma}{2\epsilon_{\mathrm{w}}V_{\mathrm{T}}}\right)\right) = \left[\left(\frac{\lambda_{\mathrm{D}}\sigma}{2\epsilon_{\mathrm{w}}V_{\mathrm{T}}}\right) + \sqrt{1+\left(\frac{\lambda_{\mathrm{D}}\sigma}{2\epsilon_{\mathrm{w}}V_{\mathrm{T}}}\right)^2}\right]^{-2} \tag{4.23}$$

$$\approx \begin{cases} \left(\frac{\lambda_{\mathrm{D}}\sigma}{\epsilon_{\mathrm{w}}V_{\mathrm{T}}}\right)^2 & , \quad \text{for } \tilde{\zeta} > 1 \\ \exp\left(-\frac{\lambda_{\mathrm{D}}\sigma}{\epsilon_{\mathrm{w}}V_{\mathrm{T}}}\right) & , \quad \text{for } \tilde{\zeta} < 1 \end{cases}. \tag{4.24}$$

Inserting these expressions in (4.21) and solving for σ we find

$$\sigma \approx \begin{cases} -3C_{\mathrm{s}}V_{\mathrm{T}}\mathrm{W}\left(\frac{\frac{\epsilon_{\mathrm{w}}}{\lambda_{\mathrm{D}}}}{3C_{\mathrm{s}}}\left[\frac{e\Gamma K_{\mathrm{SiOH}}}{c_{\mathrm{H,bulk}}V_{\mathrm{T}}\frac{\epsilon_{\mathrm{w}}}{\lambda_{\mathrm{D}}}}\right]^{1/3}\right) & , \quad \text{for } \tilde{\zeta} > 1 \\ -\frac{V_{\mathrm{T}}}{\frac{\lambda_{\mathrm{D}}}{\epsilon_{\mathrm{w}}}+\frac{1}{C_{\mathrm{s}}}}\mathrm{W}\left(\frac{e\Gamma K_{\mathrm{SiOH}}}{c_{\mathrm{H,bulk}}V_{\mathrm{T}}}\left[\frac{\lambda_{\mathrm{D}}}{\epsilon_{\mathrm{w}}}+\frac{1}{C_{\mathrm{s}}}\right]\right) & , \quad \text{for } \tilde{\zeta} < 1 \end{cases}. \tag{4.25}$$

From the expressions (4.25) it is seen that the magnitude of σ decreases monotonically with both the bulk hydronium concentration and the Debye length. Since the Debye length scales as $\lambda_D \sim I^{-1/2}$, where I is the ionic strength, we expect the magnitude of σ to increase monotonically with the salt concentration. In section 6.3.3 these trends are verified using numerical calculations.

In section 4.2 it was found that the bulk salt concentration depletes to the left of the membrane. Based only on the salt concentration we would thus expect the magnitude of the surface charge density to be very low in that region. Before making that prediction it is however necessary to know how the hydronium is distributed.

4.4 Hydronium distribution

The distribution of hydronium ions is unfortunately not easy to predict. The governing equation (2.40)

$$\boldsymbol{\nabla}\cdot\left\{\left(D_{\mathrm{H}} + D_{\mathrm{OH}}K_{\mathrm{w}}c_{\mathrm{H}}^{-2}\right)\left(\boldsymbol{\nabla}c_{\mathrm{H}} + c_{\mathrm{H}}\boldsymbol{\nabla}\phi\right) + \left(K_{\mathrm{w}}c_{\mathrm{H}}^{-2} - 1\right)c_{\mathrm{H}}\boldsymbol{u}\right\} = 0, \tag{4.26}$$

is highly nonlinear and even in the simple 1D case without advection it is not integrable.

Let us, as a starting point, consider the case where there are no salt ions in the system and the current is only carried by hydronium (and hydroxide). Because of the reaction term in (2.38) the hydronium ions are not conserved, and the system behaves in a fundamentally different way than the system where only salt ions are present.

In the problem where only salt ions are present the depletion and accumulation of ions at either side of the membrane is caused by the inability of the anions to pass through the membrane. In the case of hydronium and hydroxide the response to any beginning depletion or accumulation of ions will be a reaction that either creates or consumes water

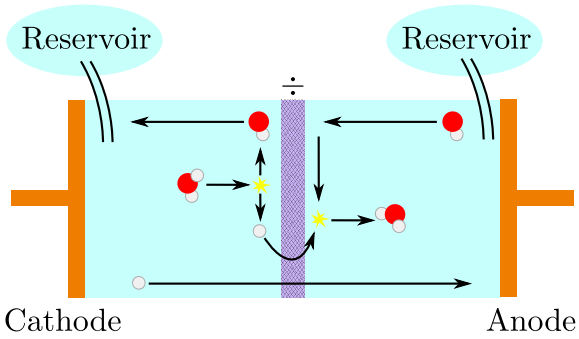

Figure 4.2: *Conduction of hydronium and hydroxide in a microchannel with a cation-selective membrane. Due to the auto-protolytic reaction of water the hydroxide can effectively circumvent the membrane.*

ions. In this way the hydroxide can effectively circumvent the membrane, and the current carrying capacity of the system will be unaffected by the presence of the ion-selective membrane (i.e. a simple linear current-voltage characteristic is found). In figure 4.2 an illustration of this is shown. The net effect of the reactions is to transport one hydroxide ion across the membrane (also one water molecule, but this is without consequence as it can freely move through the membrane).

In the general case, where also salt ions are present a more thorough treatment is required.

In previous work it has been argued, that since the concentration of salt ions is very much larger than the concentration of water ions, the charge density due to salt ions will be much larger than the charge density due to water ions [8]. This assumption was then used as a starting point for a perturbation scheme.

The assumption does indeed seem reasonable, but on closer inspection it is found not to be justified. In fact the charge densities deriving from salt and water ions are of almost equal magnitude and opposite sign.

To understand why this is the case we will again consider the case where only water ions are present. As discussed above both ions can freely pass through the membrane, and their concentrations in the channel will thus be constant and equal to the inlet concentration. We now add the salt ions to the system. Under the influence of the electric field the anions will start to deplete to the left of the membrane and accumulate to the right. The positive charge density this creates to the left of the membrane will prompt the cation and hydronium concentrations to drop, and the hydroxide concentration to increase. This is illustrated in figure 4.3.

The hydroxide at the membrane is swept left by the electric field, but because of the auto-protolytic reaction of water this does not cause the hydroxide concentration to deplete. At the reservoir, the left going hydroxide of concentration larger than $\sqrt{K_{\mathrm{w}}}$ will meet right going hydronium from the reservoir of concentration $\sqrt{K_{\mathrm{w}}}$. This will cause hydronium and hydroxide to react and form water until the product of the water ion

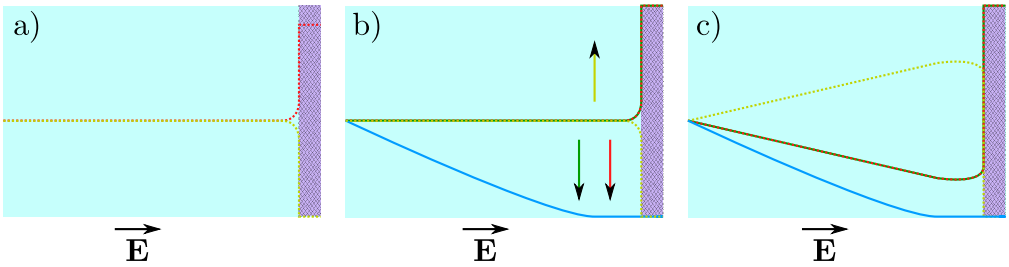

Figure 4.3: *Sketch of the channel to the left of the membrane. a) Only water ions are present in the system. Because the hydroxide (yellow) can effectively circumvent the membrane there is no depletion region and the hydronium (red) and hydroxide concentrations are constant through the channel. b) Salt ions are added. The anion (blue) concentration starts to deplete and electrostatic forces affect the cations (green) and the water ions. c) The remaining ion concentrations have been adapted to nearly satisfy electroneutrality.*

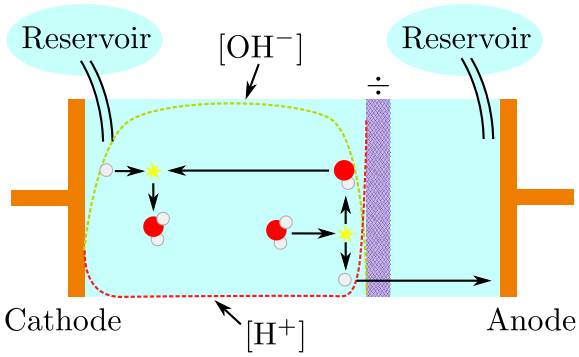

Figure 4.4: *The hydroxide created at the membrane is swept left by the electric field. Near the reservoir it reacts with hydronium to form water. The net result of these reactions is to transport one hydronium molecule from reservoir to membrane without going through the channel (also some water is moved). The resulting concentration curves for hydroxide (yellow) and hydronium (red) are shown.*

concentrations is K_w. The result of these steps is that the depletion of hydronium and the accumulation of hydroxide is broadened out to extend over most of the channel. In figure 4.4 a sketch of the relevant reactions and the resulting profiles is seen.

Since the hydroxide concentration is much larger than the hydronium concentration in most of the left channel, the water ions will contribute a significant negative space charge density in this region. This allows the cation concentration to be significantly larger than zero, and the cations will thus be able to carry a current even after the anions have depleted.

To sum up, the water ions increase the current in the system in two ways: By carrying a current themselves, and by creating a negative space charge density which allows a higher cation concentration and thus a higher cation current.

The latter of these effects was first predicted by Kharkats and is often called the exaltation effect [5, 7].

Before concluding this section we briefly return to the surface charge density. The outcome of the above analysis was that the hydronium concentration is predicted to be lowered in the left microchannel. According to (4.25) this should lead to an increase in the surface charge density. This is opposite to the tendency predicted from the salt ions alone, and as we cannot quantify the lowering of the hydronium concentration we are at a loss as to which mechanism will dominate. We can therefore only conclude that the surface charge density will vary in some way in the microchannel, and then resort to numerical calculations for the details of these variations.

Chapter 5

Numerical Modelling

The problems studied in this thesis are in general too complicated to allow for analytical solutions, and we will therefore resort to a numerical solution scheme known as the finite element method (FEM). The calculations are carried out in Comsol Multiphysics (Version 4.2), which is a commercially available FEM software.

5.1 The finite element method

The core idea in the finite element method is to discretise the problem by expanding the physical fields in a set of localised basis functions[1]. The concept of using basis functions in the study of boundary value problems is familiar from Fourier analysis, where harmonic functions are used as a basis on high symmetry geometries like rectangles, cylinders and spheres.

In the finite element method the basis functions are constructed by placing a grid over the computational domain and associating a localised function with each grid node. The value of the basis functions vary in some specified (usually polynomial) way between 1 at their own node and 0 on the neighbouring nodes. This is illustrated in figure 5.1 where a linearly varying basis function on the domain Ω is shown.

The way in which functions are represented using basis functions is most easily illustrated in 1D. In figure 5.2 the function $\sin(x)$ is shown, together with its basis function representation, for the cases of linearly and quadratically varying basis functions on a grid of node spacing 1. It is noted that the representation of $\sin(x)$ has discontinuous derivatives at the nodes. In a classical picture this would pose a problem for the solution of higher order differential equations, but as we shall later see this issue is elegantly resolved in the finite element approach. The material in this section is based on [26, 27, 28].

We consider an inhomogeneous boundary value problem, defined by a set of boundary

[1] Often called test functions in the finite element method.

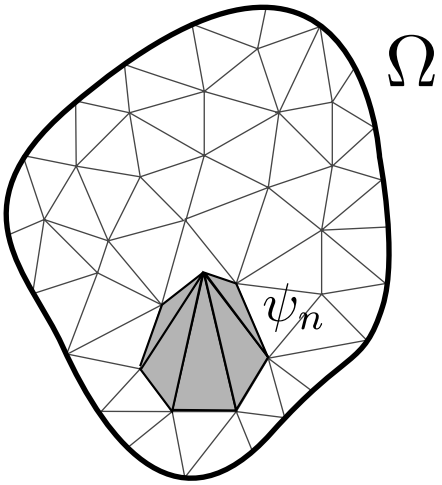

Figure 5.1: *Example of a linearly varying basis function on a 2D domain* Ω.

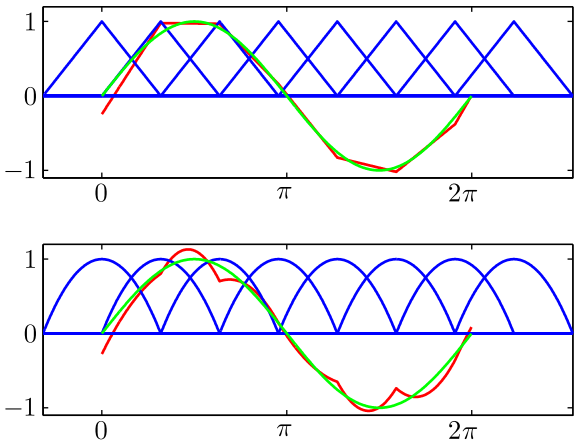

Figure 5.2: *Basis function representations of the function* $\sin(x)$ *(shown in red) for the cases of linearly and quadratically varying basis functions on a grid of node spacing 1. The basis functions are shown in blue and the function* $\sin(x)$ *itself is shown in green.*

conditions plus the PDE

$$\mathcal{L}\{g(\boldsymbol{x})\} = F(\boldsymbol{x}). \tag{5.1}$$

Here $\mathcal{L}$ is a differential operator and F is a forcing term. We also define the defect $d(\boldsymbol{x}) \equiv \mathcal{L}\{g(\boldsymbol{x})\} - F(\boldsymbol{x})$, which is zero when (5.1) is satisfied.
It is assumed that g can be approximately expressed in terms of a finite basis $\{\psi_n\}$

$$g(\boldsymbol{x}) = \sum_n c_n \psi_n, \tag{5.2}$$

where c_n are the expansion coefficients. Since the basis functions nearly span the function space, equation (5.1) will be approximately satisfied if the projection of the defect $d(\boldsymbol{x})$ on every basis function vanishes. i.e.

$$\langle \psi_m, d(\boldsymbol{x}) \rangle = 0 \quad , \quad \text{For all } m, \tag{5.3}$$

where the inner product is defined as $\langle a(\boldsymbol{x}), b(\boldsymbol{x}) \rangle \equiv \int_\Omega a(\boldsymbol{x}) b(\boldsymbol{x})\, \mathrm{d}\boldsymbol{x}$. A solution satisfying (5.3) is called a weak solution of the boundary value problem[2]. An important feature

[2]In contrast a solution satisfying (5.1) is called a strong solution of the boundary value problem.

of this weak formulation of the problem is that the smoothness of g is not of critical importance. The reason for this is that any singularities in the defect, resulting from kinks in g, are immediately integrated away. Inserting the defect in (5.3) we obtain

$$\left\langle \psi_m, \mathcal{L} \sum_n c_n \psi_n \right\rangle = \langle \psi_m, F(\boldsymbol{x}) \rangle \quad , \quad \text{For all } m, \tag{5.4}$$

which, in the important case where $\mathcal{L}$ is linear, reduces to

$$\sum_n c_n \langle \psi_m, \mathcal{L}\psi_n \rangle = \langle \psi_m, F(\boldsymbol{x}) \rangle \quad , \quad \text{For all } m. \tag{5.5}$$

This system of equations can be written as a matrix problem

$$\boldsymbol{K}\boldsymbol{c} = \boldsymbol{f}, \tag{5.6}$$

where the stiffness matrix $\boldsymbol{K}$ has elements $K_{nm} = \langle \psi_m, \mathcal{L}\psi_n \rangle$, the vector $\boldsymbol{c}$ contains the coefficients c_n and the elements in $\boldsymbol{f}$ are given as $\langle \psi_m, F(\boldsymbol{x}) \rangle$. Obtaining the weak solution to (5.1) is thus just a matter of solving the matrix equation (5.6) for the coefficient vector $\boldsymbol{c}$.

It is noted that the reformulation of the problem to a simple matrix problem hinges crucially on the linearity of $\mathcal{L}$.

In the above treatment no mention was made of the boundary conditions, although they are arguably the most important part of a boundary value problem. A quite natural way of implementing the boundary conditions is provided by rewriting (5.3) a bit. To do this we will assume that (5.1) can be written as a continuity equation

$$\boldsymbol{\nabla} \cdot \boldsymbol{\Gamma} = F(\boldsymbol{x}). \tag{5.7}$$

This may seem restrictive, but in reality almost every equation encountered in physics is a continuity equation of some kind. Inserting (5.7) in (5.3) we get

$$\langle \psi_m, \boldsymbol{\nabla} \cdot \boldsymbol{\Gamma} - F(\boldsymbol{x}) \rangle = \int_\Omega \psi_m \boldsymbol{\nabla} \cdot \boldsymbol{\Gamma} - \psi_m g(\boldsymbol{x}) \, \mathrm{d}\boldsymbol{x} = 0. \tag{5.8}$$

Using that $\boldsymbol{\nabla} \cdot \{\psi_m \boldsymbol{\Gamma}\} = \psi_m \boldsymbol{\nabla} \cdot \boldsymbol{\Gamma} + \boldsymbol{\nabla}\psi_m \cdot \boldsymbol{\Gamma}$ a part of the integral can be converted to an integral over the boundary

$$\int_\Omega \psi_m \boldsymbol{\nabla} \cdot \boldsymbol{\Gamma} - \psi_m F(\boldsymbol{x}) \, \mathrm{d}\boldsymbol{x} = 0 \tag{5.9a}$$

$$\Leftrightarrow \int_\Omega \boldsymbol{\nabla} \cdot \{\psi_m \boldsymbol{\Gamma}\} - \boldsymbol{\nabla}\psi_m \cdot \boldsymbol{\Gamma} - \psi_m F(\boldsymbol{x}) \, \mathrm{d}\boldsymbol{x} = 0 \tag{5.9b}$$

$$\Leftrightarrow \int_{\partial\Omega} \psi_m \boldsymbol{n} \cdot \boldsymbol{\Gamma} \, \mathrm{d}\boldsymbol{x} + \int_\Omega -\boldsymbol{\nabla}\psi_m \cdot \boldsymbol{\Gamma} - \psi_m F(\boldsymbol{x}) \, \mathrm{d}\boldsymbol{x} = 0. \tag{5.9c}$$

In (5.9c) Neumann boundary conditions can simply be implemented by replacing $\boldsymbol{n} \cdot \boldsymbol{\Gamma}$ in the surface integral with the appropriate condition. Another advantage of the formulation in (5.9c) is that it does not include derivatives of $\boldsymbol{\Gamma}$, and as a consequence shape functions of a lower order can be used to construct the basis functions.

Typically, a boundary value problem will also include Dirichlet boundary conditions. Dirichlet conditions can be considered as equations of constraint on the dependent variables and written as

$$M = 0, \tag{5.10}$$

where M depends on the dependent variables. We multiply the equation of constraint with a Lagrangian multiplier λ, and after a bit of math[3] a modified version of the governing equation is obtained

$$\boldsymbol{\nabla} \cdot \boldsymbol{\Gamma} = F(\boldsymbol{x}) + \sum_i \sum_n \lambda \frac{\partial M}{\partial c_{i,n}}. \tag{5.11}$$

Here $c_{i,n}$ is the coefficient to the n'th basis function of the i'th dependent variable. In the common case where the dependent variables enter linearly in M the constraint force just becomes

$$\sum_i \sum_n \lambda \frac{\partial M}{\partial c_{i,n}} = \sum_i \sum_n \lambda a_i \psi_{i,n}, \tag{5.12}$$

where a_i is the coefficient to the i'th dependent variable in the constraint term M.

The Lagrangian multiplier λ is a field which lives only where the constraint is defined, and it too can be expanded in a set of basis functions. The equation of constraint can thus be written

$$\langle \psi_{\lambda,m}, M \rangle = 0, \quad \text{For all } m, \tag{5.13}$$

where $\psi_{\lambda,m}$ are the basis functions of λ. Rewriting (5.11) as done in (5.9) and adding (5.13) a single matrix problem is obtained for the solution of the boundary value problem.

As earlier noted, the approach outlined here only works for linear problems. For nonlinear problems the equations are linearised around an operation point and the obtained solution is used to find a new operating point. This is continued until a self-consistent solution is found.

The success of this procedure is highly dependent on the initial operating point. When dealing with very nonlinear problems it is therefore often necessary to introduce the nonlinearity slowly.

[3]The governing equation is treated as deriving from an unknown variational principle and the approach in [29] pp. 1065 is followed.

5.2 Comsol

Comsol Multiphysics is a GUI based software implementation of the finite element method. It includes diverse drawing tools for the definition of physical domains as well as a number of automated meshing sequences. Because Comsol is primarily directed towards users in the industry a large number of predefined physics modules are included in the software. In these modules the relevant governing equations and constitutive relations for the study of a specific physical problem are already defined, and often the user needs only define the geometry and choose from a list of boundary conditions.

While convenient and fast there are a few drawbacks to using the predefined modules: When using the modules it is not always fully transparent which equations Comsol is really solving, and the modules may not be flexible enough to allow for the desired implementation of the physical problem.

For more flexibility and greater transparency it is possible to define the governing equations and boundary conditions directly in weak form[4]. In this work we will be using this option, as a great deal of flexibility is required in the definition of some of the considered problems.

5.3 Mesh Convergence

The whole finite element method hinges on the assumption that the basis functions approximately span the relevant function space. If this is not the case the matrix problem (5.6) might still be solvable, but the obtained solution can deviate significantly from the correct physical solution.

In the finite element method the ability of the basis functions to span a function space is determined by the coarseness of the mesh. A suitable mesh should thus be very fine in regions where the physical fields vary over small distances, while it can be quite coarse in regions with small variations of the fields. Some physical intuition about the expected solution can therefore greatly help in the task of defining a suitable mesh.

To verify that a given mesh is sufficiently fine to resolve the physical fields a mesh convergence test should be made. In a mesh convergence test the physical problem is solved for different meshes of varying coarseness, and a characteristic parameter obtained from the solution (e.g. the current in the system) is plotted versus the coarseness. For very coarse meshes the mesh will have a direct effect on the problem and the chosen parameter will vary a lot when changing coarseness. As the mesh is refined the parameter will converge towards a certain value, signifying that the mesh adequately resolves the physical fields. The coarsest mesh giving the converged parameter value will then often be chosen for the rest of the calculations. In figure 5.3 a mesh convergence plot is shown, where the mesh size is varied by scaling the chosen mesh. It is seen that the chosen mesh (scaling=1) is sufficiently refined to resolve the relevant physics.

[4]Also, certain types of PDE's can be defined in coefficient form.

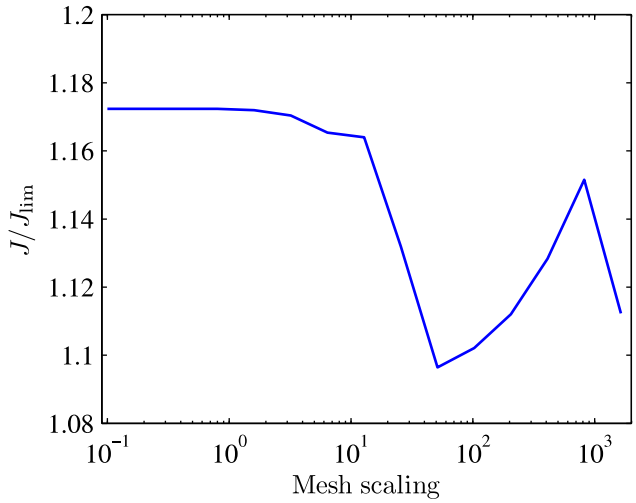

Figure 5.3: *Mesh convergence plot. The current trough a 1D system is plotted for different mesh sizes. For very fine meshes the current is seen to converge towards a limiting value, while it varies greatly with the mesh size for the coarser meshes. The mesh is varied by multiplying the chosen mesh size with a scaling parameter.*

Mesh convergence tests have been carried out for each of the simulations in the remainder of the thesis.

Chapter 6

An effective 1D model for ion transport

A characteristic feature of the systems studied in this thesis is the thin screening layers which develop at the microchannel surfaces and at the membrane interface. The Debye length is often taken to be the characteristic size of these screening layers, but as shown in section 4.1 the characteristic length can be orders of magnitude smaller than the Debye length when the magnitude of the surface charge is large.

The small length scale set by the screening layers is a serious issue when meshing the physical domains with typical dimensions $R \sim 0.5\,\mu\text{m} - 5\,\mu\text{m}$ and $L \sim 100\,\mu\text{m} - 1\,\text{mm}$. For instance it would require around 500 billion mesh elements to mesh a $5\,\mu$m by 1 mm domain with elements of side length 0.1 nm. The number of required elements can be significantly reduced by varying the coarseness of the mesh over the domain, but the disparate length scales set by the domain and the screening lengths do introduce a very high lower limit to the number of mesh elements.

This issue motivates us to look for ways of simplifying the modelling of the physical problem. To this end we note that most of the complicated physics happens close to the membrane and in the extended space charge region. Outside this region it might thus be possible to give an adequate description of the physics using a much simpler model. In this chapter we will follow this line of thought and develop a simple 1D model describing the physics well away from the membrane and a 1D model describing the physics inside the membrane. Later we will couple these 1D models to a full 2D model near the membrane.

6.1 Modelling of the effective 1D problem

We consider a section of the microchannel which is far away from the membrane, so that its influence is not felt directly by the salt ions or the velocity field. In the simplest case, where the salt concentration and the surface charge density is constant along the length of the section, this means that the current densities and the velocity field will be unidirectional. The vanishing of the radial current density implies that the ions are

radially equilibrated at all points in the channel section.

In the general case, where the salt concentration and the surface charge density can vary along the section, the amount of current which is carried in the bulk relative to the current in the screening layers will change along the channel length. It follows that a radial current must exist. If the radial transport is much faster than the axial transport it may however still be justified to assume radial equilibrium of the ions.

Below we will use this assumption to develop a 1D model for the ion transport, and subsequently we will estimate the regime in which the model is valid.

The electrical potential is split up in an axial part which depends only on x and an equilibrium potential which depends on both x and r.

$$\phi(x,r) = \phi_{\mathrm{ax}}(x) + \phi_{\mathrm{eq}}(x,r). \tag{6.1}$$

Due to the assumption of transverse equilibrium the ion concentrations can then be written as

$$c_{\pm}(x,r) = k_{\pm}(x) e^{\mp \tilde{\phi}_{\mathrm{eq}}(x,r)}, \tag{6.2a}$$

$$c_{\mathrm{H}}(x,r) = h(x) e^{-\tilde{\phi}_{\mathrm{eq}}(x,r)}, \tag{6.2b}$$

where $k_{\pm}(x) \equiv c_{\pm}(x,0) e^{\pm \tilde{\phi}_{\mathrm{eq}}(x,0)}$ and $h(x) \equiv c_{\mathrm{H}}(x,0) e^{\tilde{\phi}_{\mathrm{eq}}(x,0)}$. The Poisson equation

$$\epsilon_{\mathrm{w}} \nabla^2 \phi = \epsilon_{\mathrm{w}} \left[\partial_x^2 \phi_{\mathrm{ax}} + \nabla^2 \phi_{\mathrm{eq}} \right] = e \left[c_- - c_+ + \frac{K_{\mathrm{w}}}{c_{\mathrm{H}}} - c_{\mathrm{H}} \right], \tag{6.3}$$

is split up into an axial equation

$$\epsilon_{\mathrm{w}} \partial_x^2 \phi_{\mathrm{ax}} = e \left(k_- + \frac{K_{\mathrm{w}}}{h} \right) - e \left(k_+ + h \right), \tag{6.4}$$

and an equation for the equilibrium potential

$$\epsilon_{\mathrm{w}} \nabla^2 \phi_{\mathrm{eq}} = e \left(k_- + \frac{K_{\mathrm{w}}}{h} \right) \left(e^{\tilde{\phi}_{\mathrm{eq}}(x,r)} - 1 \right) - e \left(k_+ + h \right) \left(e^{-\tilde{\phi}_{\mathrm{eq}}(x,r)} - 1 \right). \tag{6.5}$$

Here the salt ions have been assumed monovalent.
The transverse variations of ϕ_{eq} are much larger than the axial variations, so to a good approximation we can substitute $\nabla^2 \phi_{\mathrm{eq}} \approx \partial_r^2 \phi_{\mathrm{eq}} + \frac{1}{r} \partial_r \phi_{\mathrm{eq}}$ in the above equation. The radial and the axial problems thus only couple through $k_{\pm}$ and h.

The continuity equation for the dissolved species reads

$$\boldsymbol{\nabla} \cdot \boldsymbol{J}_i = \partial_x J_{i,\mathrm{x}} + \frac{1}{r} \partial_r \left\{ r J_{i,\mathrm{r}} \right\} = 0, \tag{6.6}$$

where $i \in \{+, -, \mathrm{w}\}$. Averaging this equation over the cross-section of the channel yields a continuity equation for the average axial current density

$$\left\langle \boldsymbol{\nabla} \cdot \boldsymbol{J}_i \right\rangle = \partial_x \left\langle J_{i,\mathrm{x}} \right\rangle = 0. \tag{6.7}$$

The average axial current density is

$$\langle J_{\pm,\mathrm{x}}\rangle = D_\pm \left\langle -\partial_x c_\pm \mp c_\pm \partial_x(\tilde{\phi}_{\mathrm{ax}} + \tilde{\phi}_{\mathrm{eq}}) \right\rangle + \langle c_\pm u\rangle \tag{6.8}$$

$$= D_\pm(-\partial_x k_\pm \mp k_\pm \partial_x \tilde{\phi}_{\mathrm{ax}}) \left\langle e^{\mp\tilde{\phi}_{\mathrm{eq}}} \right\rangle + k_\pm \left\langle u e^{\mp\tilde{\phi}_{\mathrm{eq}}} \right\rangle, \tag{6.9}$$

for the salt ions, and for the water ions it is

$$\langle J_{\mathrm{w,x}}\rangle = -\left(D_{\mathrm{H}} \left\langle e^{-\tilde{\phi}_{\mathrm{eq}}} \right\rangle + D_{\mathrm{OH}} \frac{K_{\mathrm{w}}}{h^2} \left\langle e^{\tilde{\phi}_{\mathrm{eq}}} \right\rangle \right)(\partial_x h + h\partial_x \phi_{\mathrm{ax}}) + \left(h \left\langle u e^{-\tilde{\phi}_{\mathrm{eq}}} \right\rangle - \frac{K_{\mathrm{w}}}{h} \left\langle u e^{\tilde{\phi}_{\mathrm{eq}}} \right\rangle \right). \tag{6.10}$$

The averaged Boltzmann factors $\left\langle e^{\mp\tilde{\phi}_{\mathrm{eq}}} \right\rangle$ can be found as a function of $k_\pm$ and h by solving (6.5). In the following we will often use J_i as a shorthand for the average current density $\langle J_i\rangle$.

In order to find the axial velocity field u we have to solve the Stokes equation. We do this assuming unidirectionality of the flow and therefore only the axial component of the equation is considered

$$\begin{aligned} 0 =& -\partial_x p + \eta\nabla^2 u - \rho_{\mathrm{el}}\partial_x \phi_{\mathrm{ax}} \\ \Leftrightarrow 0 =& -\partial_x p + \eta\nabla^2 u + \epsilon_{\mathrm{w}} \left(\partial_x^2 \phi_{\mathrm{ax}} + \partial_x^2 \phi_{\mathrm{eq}} + \frac{1}{r}\partial_r \left\{ r\partial_r \phi_{\mathrm{eq}} \right\} \right)(\partial_x \phi_{\mathrm{ax}} + \partial_x \phi_{\mathrm{eq}}) = 0. \end{aligned} \tag{6.11}$$

The pressure gradient term $\partial_x p$ ensures that the velocity field is incompressible when averaged over the cross-section. Any other purely x-dependent terms like $\epsilon_{\mathrm{w}}\partial_x^2\phi_{\mathrm{ax}}\partial_x\phi_{\mathrm{ax}}$ can be absorbed into the pressure gradient. Assuming that the axial variations of u and ϕ_{eq} are negligible equation (6.11) takes the form

$$\partial_x p = \frac{1}{r}\partial_r \left\{ r\partial_r \left\{ \eta u + \epsilon_{\mathrm{w}}\phi_{\mathrm{eq}}\partial_x\phi_{\mathrm{ax}} \right\} \right\}, \tag{6.12}$$

which can be integrated to give

$$u = -\frac{\epsilon_{\mathrm{w}}\partial_x\phi_{\mathrm{ax}}}{\eta}\left(\phi_{\mathrm{eq}}(x,r) - \zeta(x)\right) - \frac{1}{4}\frac{\partial_x p}{\eta}\left(R^2 - r^2\right). \tag{6.13}$$

Requiring the average velocity over the cross-section to be zero we finally get

$$u(x,r) = -\frac{\epsilon_{\mathrm{w}}\partial_x\phi_{\mathrm{ax}}}{\eta}\left[\left(\phi_{\mathrm{eq}}(x,r) - \zeta(x)\right) - \left\langle \phi_{\mathrm{eq}}(x,r) - \zeta(x) \right\rangle 2\left(1 - \frac{r^2}{R^2}\right) \right]. \tag{6.14}$$

This expression for the velocity is separable into a part which can be found by solving the radial problem (the part in square brackets), and a part, $\partial_x\phi_{\mathrm{ax}}$, which pertains to the axial problem. Introducing $w \equiv -\frac{\eta}{\epsilon_{\mathrm{w}}\partial_x\phi_{\mathrm{ax}}}u$ the average of the velocity times the Boltzmann factor can thus be written

$$\left\langle u e^{\tilde{\phi}_{\mathrm{eq}}} \right\rangle = -\frac{\epsilon_{\mathrm{w}}\partial_x\phi_{\mathrm{ax}}}{\eta}\left\langle w e^{\tilde{\phi}_{\mathrm{eq}}} \right\rangle, \tag{6.15}$$

where the term in brackets on the right hand side can be found by solving the radial problem (6.5).

Having reformulated the axisymmetric 3D problem into an effective 1D problem we will now consider the range of validity of the model. The central assumption used above was that the radial transport happens on a much shorter time scale than the axial transport, i.e.

$$\tau_{\mathrm{r}} \ll \tau_{\mathrm{x}}. \tag{6.16}$$

Dimensional analysis gives that

$$\tau_{\mathrm{r}} \sim \frac{R^2}{D} \quad \text{and} \quad \tau_{\mathrm{x},1} \sim \frac{L_0^2}{D}, \quad \tau_{\mathrm{x},2} \sim \frac{L_0}{u_0}, \tag{6.17}$$

where L_0 is some characteristic axial length scale and u_0 is a characteristic velocity. There are two time scales for the axial transport since both advection and migration can be important. A natural choice of axial length scale is offered by scaling the derivative of the relevant concentration field

$$\frac{1}{L_0} \sim \frac{\partial_x c}{c} = \partial_x \ln(c). \tag{6.18}$$

The 1D model should thus be valid when

$$R^2 \ll L_0^2 \quad \Leftrightarrow \quad R^2 \left(\partial_x \ln(c)\right)^2 \ll 1, \tag{6.19}$$

and

$$\frac{R^2}{D} \partial_x \ln(c) u_0 << 1. \tag{6.20}$$

6.1.1 1D model of the membrane

Inside the membrane any transverse variations of the fields can be neglected since the pore size is of the order of nanometers. Taking the porosity ϵ_{P} and the permittivity ϵ_{m} of the membrane into account the Poisson equation therefore becomes

$$\epsilon_m \partial_x^2 \phi = \epsilon_{\mathrm{P}} e \left(c_- + \frac{\sqrt{K_{\mathrm{w}}}}{c_{\mathrm{H}}} - c_+ - c_{\mathrm{H}} \right) - \rho_{\mathrm{m}}. \tag{6.21}$$

The tortuosity τ of the membrane effectively decreases the diffusivity so the current densities become

$$J_i = \frac{D_i}{\tau} \epsilon_{\mathrm{P}} \left(-\partial_x c_i \mp c_i \partial_x \tilde{\phi} \right), \tag{6.22}$$

where $i \in \{+, -, \mathrm{H}, \mathrm{OH}\}$.

6.2 Implementation of the 1D model

By construction the developed 1D model is only valid in a limited part of the system. The discrepancy between the 1D and full 2D model is however not expected to affect the physics of the problem fundamentally, as their primary difference is that their radial distributions differ slightly. Well aware that it will introduce an error in the results, we will therefore attempt to model the entire system using the effective 1D model.

In the 1D model the problem is fully specified by the equations (6.4), (6.7), (6.21) and (6.22) plus appropriate boundary conditions. The average currents depend on the equilibrium potential through the average Boltzmann factors. Unfortunately, equation (6.5) is not integrable in a cylindrical geometry and it is therefore necessary to find the average Boltzmann factors via numerical calculations.

For a given channel radius we solve the 1D equation (6.5) on the cross-section for different values of $k_\pm$ and h and tabulate the values of $\left\langle e^{\pm\tilde{\phi}_{\mathrm{eq}}}\right\rangle$ and $\left\langle we^{\pm\tilde{\phi}_{\mathrm{eq}}}\right\rangle$. At the centre axis the symmetry boundary condition $\boldsymbol{n}\cdot\boldsymbol{\nabla}\phi_{\mathrm{eq}}=0$ is used and at the channel wall the elctrostatic boundary condition $\epsilon_{\mathrm{w}}\boldsymbol{n}\cdot\boldsymbol{\nabla}\phi_{\mathrm{eq}}=\sigma$ is used. Here the unit normal vector $\boldsymbol{n}$ denotes the vector pointing outwards from the domain.

The equation (6.5) only depends on $k_\pm$ and h through $k_- + \frac{K_{\mathrm{w}}}{h}$ and $k_+ + h$, so for a constant surface charge density it is sufficient to sweep over the two parameters $k_- + \frac{K_{\mathrm{w}}}{h}$ and $k_+ + h$. If, however, the dynamic surface charge density (2.43) is used a sweep over all three of the parameters $k_\pm$ and h is necessary.

To make $\left\langle e^{\pm\tilde{\phi}_{\mathrm{eq}}}\right\rangle$ and $\left\langle we^{\pm\tilde{\phi}_{\mathrm{eq}}}\right\rangle$ available to COMSOL as continuous and differentiable functions COMSOL is coupled to MATLAB, in which the average Boltzmann factors are cubically interpolated.

The simplest way to couple the equations in the microchannels to those in the membrane is to simply let the expression for the space charge density and the expression for the current density depend on position. This can be done by defining a function

$$f(x,a,b)=\begin{cases} a\ , & \text{For } x \text{ outside the membrane} \\ b\ , & \text{For } x \text{ inside the membrane} \end{cases}. \tag{6.23}$$

The current densities are then written

$$J_i = D_i f\left(x,\left\langle e^{\mp\tilde{\phi}_{\mathrm{eq}}}\right\rangle,\frac{\epsilon_{\mathrm{P}}}{\tau}\right)\left(-\partial_x k_i \mp k_i\partial_x\phi\right) - f\left(x,1,0\right)k_i\frac{\epsilon_{\mathrm{w}}\partial_x\phi_{\mathrm{ax}}}{\eta}\left\langle we^{\tilde{\phi}_{\mathrm{eq}}}\right\rangle, \tag{6.24}$$

with $i\in\{+,-,\mathrm{H},\mathrm{OH}\}$. Likewise, the Poisson equation becomes

$$\partial_x^2\phi = f\left(x,\frac{1}{\epsilon_{\mathrm{w}}},0\right)\left[e\left(k_- + \frac{K_{\mathrm{w}}}{h}\right) - e\left(k_+ + h\right)\right] \tag{6.25}$$

$$+ f\left(x,0,\frac{1}{\epsilon_{\mathrm{m}}}\right)\left[\epsilon_{\mathrm{P}}e\left(k_- + \frac{\sqrt{K_{\mathrm{w}}}}{h} - k_+ - h\right) - \rho_{\mathrm{m}}\right]. \tag{6.26}$$

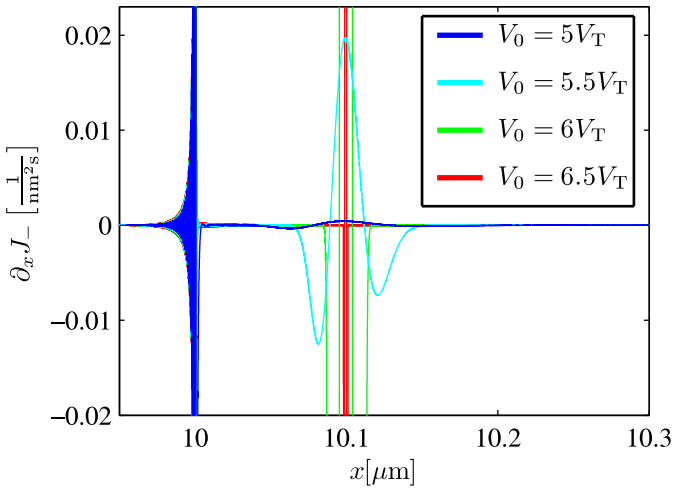

Figure 6.1: *The divergence of J_- plotted close to the membrane ($x = 10\,\mu$m). The small error initiated at $V_0 = 5V_\mathrm{T}$ increases exponentially as the voltage increases. The deviation from zero at $x = 10\,\mu$m is caused by the membrane, but it is not a problem as it does not grow and the current is conserved from one side of it to the other.*

These formulations ensure that the current densities and concentration fields as well as the electric field and the potential are continuous throughout the system.

As the membrane is assumed to have infinite hydraulic resistance the flow has to vanish at the membrane interface. A crude estimate gives that the axial flow vanishes over a distance $R/4$ close to the membrane. This effect is implemented by multiplying the velocity with a sigmoid function.

The primary aim of the calculations is to find the I-V curves for the system. To do this the problem is solved for varying bias voltages. This also has the advantage that it slowly increases the degree of nonlinearity, and it thus ensures good starting guesses for the heavily biased systems.

In Comsol a parametric sweep, for instance over the voltage, is made on the basis of a specified list of parameters. By default Comsol has a routine which often enables it to do a parametric sweep comparatively fast. In this routine the solutions are not fully converged before Comsol jumps on to the next parameter value, but in exchange also parameter values between those in the parameter list are used. This routine turns out to cause problems in our system as numerical instabilities accumulate during the parametric sweep. This is illustrated in figure 6.1, where the divergence of J_- is plotted versus the position close to the membrane interface for increasing bias voltages. At $V_0 = 5V_\mathrm{T}$ a small oscillatory error emerges, and as the voltage increases it is seen to increase exponentially in magnitude. This eventually causes the simulation to break down.

There is no built in feature for disabling this problematic routine, but the problem can be fixed by including a dummy parameter in the sweep, as Comsol is unable to do the routine in multi-parameter sweeps.

6.3 Results

To be able to properly discriminate between the consequences of different physical effects a number of calculations including increasingly complex physics are carried out. In succession we consider the cases of zero, constant and dynamic surface charge density.

6.3.1 Zero surface charge density

The case of zero surface charge actually describes a very wide channel, where surface effects can be neglected, connected to a membrane. In this effectively translation invariant system the 1D equations exactly describe the physics (i.e. if we disregard the possibility of symmetry breaking).

The calculations are carried out both with and without water ions included in the model. In figure 6.2 the electric current densities are plotted for both cases. The currents are normalised with the classical limiting current density $J_{\text{lim}} = 2\frac{eD_+c_0}{L_{\text{ic}}}$, c.f. equation (4.12). The inlet concentration was taken as $c_0 = 1\,\text{mM}$, the inlet pH as 7 and the lengths were $L_{\text{ic}} = 1\,\text{mm}$, $L_{\text{m}} = 100\,\mu\text{m}$ and $L_{\text{oc}} = 1\,\text{mm}$.

Without water ions the current exceeds the classical limiting current slightly for large voltages. This is due to the formation of an extended space charge layer in front of the membrane. To illustrate this the cation concentration and the space charge density in the left channel have been plotted in figure 6.3.

For the case with hydronium both the cation current J_+ and the total current J_{tot} are plotted in 6.2. The current is increased above the current in the hydronium-free system by two effects as discussed in section 4.4. One effect is that the hydroxide can effectively circumvent the membrane, and a large water ion current can thus run in the system as the current is only slightly hindered by the membrane. The other effect is that a larger cation current can run in the system, because the cation concentration can deviate more from the anion concentration when screened by the water ions (the exaltation effect). The charge density deriving from water ions can be very large as seen in figure 6.5. The charge density from the salt ions will however almost cancel it out, so that the total charge density (figure 6.4) resembles the charge density found without water ions in the system (figure 6.3).

6.3.2 Constant surface charge density

We now go on to consider the slightly more complicated case of a microchannel with constant, finite surface charge density. Simulations have been made for a model excluding water ions and flow, for a model including water ions but excluding flow and for a model including both flow and water ions. The resulting I-V curves are shown in figure 6.6, where also the analytical expression (4.20) is plotted for comparison. Again, the inlet concentration was taken as $c_0 = 1\,\text{mM}$, the inlet pH as 7 and the lengths were $L_{\text{ic}} = 1\,\text{mm}$, $L_{\text{m}} = 100\,\mu\text{m}$ and $L_{\text{oc}} = 1\,\text{mm}$. A channel of radius $R = 1\,\mu\text{m}$ with surface charge density $\sigma = 1\,\text{mC/m}^2$ was used.

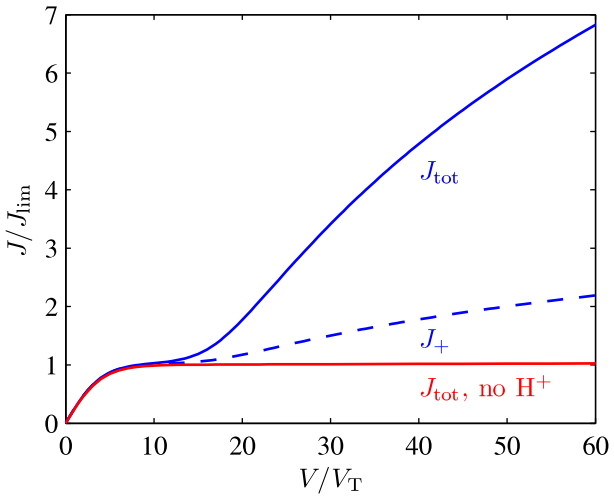

Figure 6.2: *Zero surface charge. Red: The current density for a model excluding water ions. For high voltages the current exceeds the limiting current slightly. Blue dashed: The cation current density for a model including water ions. The exaltation effect increases the cation current above the current found without water ions. Blue: The total current for a model including water ions. On top of the cation current there is a significant current of water ions. Parameters:* $\sigma = 0$, $c_0 = 1\,\mathrm{mM}$, pH $= 7$, $L_{\mathrm{ic}} = 1\,\mathrm{mm}$, $L_{\mathrm{m}} = 100\,\mu\mathrm{m}$, $L_{\mathrm{oc}} = 1\,\mathrm{mm}$.

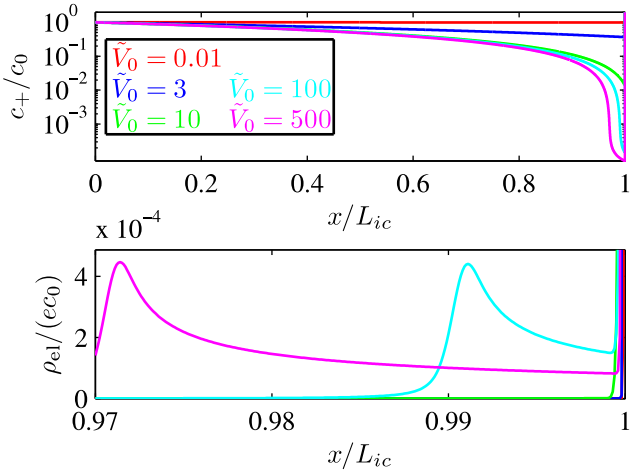

Figure 6.3: *Model with zero surface charge and without water ions. Top: Axial cation concentration along the inlet channel. Bottom: Axial space charge density near the membrane. Parameters:* $\sigma = 0$, $c_0 = 1\,\mathrm{mM}$, $L_{\mathrm{ic}} = 1\,\mathrm{mm}$, $L_{\mathrm{m}} = 100\,\mu\mathrm{m}$, $L_{\mathrm{oc}} = 1\,\mathrm{mm}$.

In figure 6.7 the cation concentration and the pH have been plotted for varying bias voltages. This time also the concentration in the membrane and in the right channel have been plotted. The depletion region is seen to extend much further out into the left channel than for the case of zero surface charge. Also, the hydronium concentration is seen to be affected by the depletion region.

Remarkably, the current density for the case of zero surface charge is larger than for the case of constant surface charge. It seems strange that the existence of the extra conduction channel, which the screening layer constitute, would mean a decrease in the current. To understand why this is the case we must first consider the form of the depletion regions in the two cases.

In the zero surface charge case the space charge region forms, because the energetic cost of having a region of finite space charge is offset by the amount of potential energy which the cations can lose by going from the cathode to the anode. The depletion region is narrow in this case to minimize the amount of unscreened charge in the system.

In the case of a finite surface charge density surface conduction provides a way for

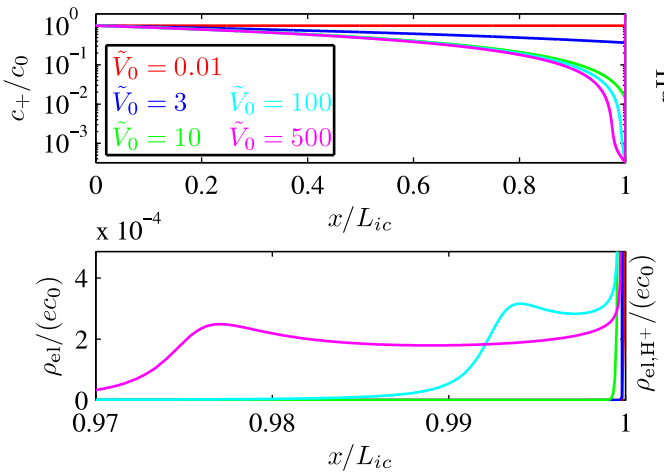

Figure 6.4: *Model with zero surface charge including water ions. Top: Axial cation concentration along the inlet channel. Bottom: Axial space charge density near the membrane. Parameters:* $\sigma = 0$, $c_0 = 1\,\mathrm{mM}$, pH $= 7$, $L_{\mathrm{ic}} = 1\,\mathrm{mm}$, $L_{\mathrm{m}} = 100\,\mu\mathrm{m}$, $L_{\mathrm{oc}} = 1\,\mathrm{mm}$.

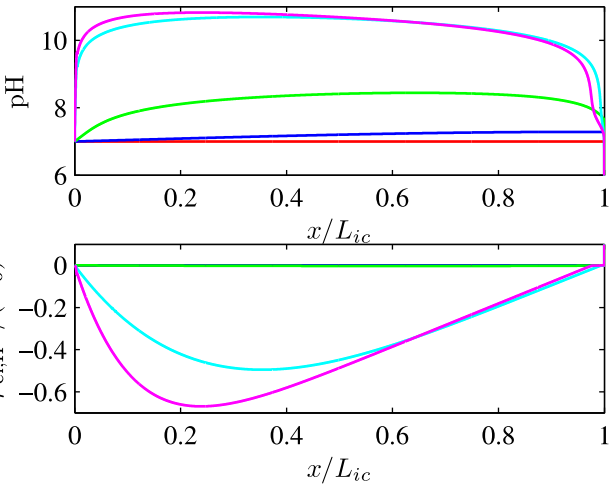

Figure 6.5: *Model with zero surface charge including water ions. Top: Axial pH along the inlet channel. Bottom: Axial space charge density due to the water ions along the inlet channel. Parameters:* $\sigma = 0$, $c_0 = 1\,\mathrm{mM}$, pH $= 7$, $L_{\mathrm{ic}} = 1\,\mathrm{mm}$, $L_{\mathrm{m}} = 100\,\mu\mathrm{m}$, $L_{\mathrm{oc}} = 1\,\mathrm{mm}$.

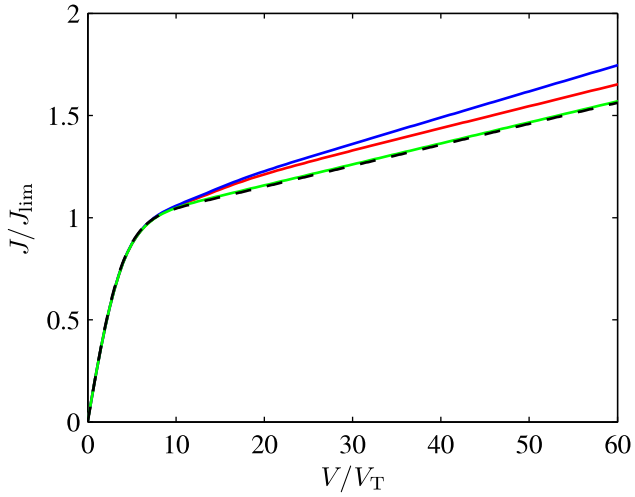

Figure 6.6: *I-V curves for model with surface charge* $\sigma = 0.001\,\mathrm{C/m^2}$. *Blue: Model including advection and hydronium. Red: Model including hydronium and excluding advection. Green: Model excluding advection and hydronium. Black dashed: The analytical expression* (4.20). *Parameters:* $\sigma = 1\,\mathrm{mC/m^2}$, $c_0 = 1\,\mathrm{mM}$, pH $= 7$, $L_{\mathrm{ic}} = 1\,\mathrm{mm}$, $L_{\mathrm{m}} = 100\,\mu\mathrm{m}$, $L_{\mathrm{oc}} = 1\,\mathrm{mm}$, $R = 1\,\mu\mathrm{m}$.

the cations of going through the depletion region without creating a space charge density. Therefore the depletion region can extend much further out than when there is no surface charge. This has the effect of bringing the depletion region closer to the reservoir, and as a

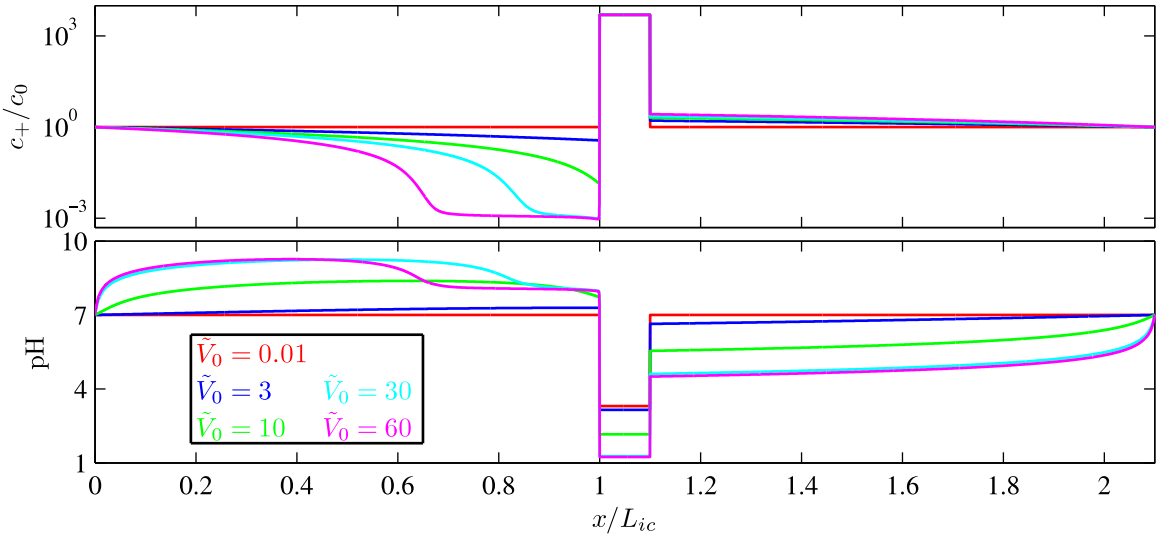

Figure 6.7: *Axial concentration profiles for model with surface charge* $\sigma = 0.001\,\mathrm{C/m^2}$. *Top: the cation concentration which is seen to have an extended depletion region. Bottom: The pH distribution is seen to depend on the depletion zone. Parameters:* $\sigma = 1\,\mathrm{mC/m^2}$, $c_0 = 1\,\mathrm{mM}$, pH = 7, $L_{\mathrm{ic}} = 1\,\mathrm{mm}$, $L_{\mathrm{m}} = 100\,\mu\mathrm{m}$, $L_{\mathrm{oc}} = 1\,\mathrm{mm}$, $R = 1\,\mu\mathrm{m}$.

result a comparatively large diffusion current of anions can run. This makes the depletion of anions less pronounced than in the case of zero surface charge density.

We now go on to consider the influence of the depletion region on the water ions. In the depletion region the anion concentration is very low and as a consequence the hydronium concentration is forced down and the hydroxide concentration is forced up. To re-equilibrate the auto-protolytic reaction water ions will then be created until their product is K_{w} again. The result of these two steps is that the hydronium concentration is increased and the hydroxide concentration is decreased in the depletion region relative to the concentration to the left of the depletion region. This effect can be seen in figure 6.7 (bottom), and it effectively lowers the magnitude of the water ion space charge density in the depletion region. The magnitude of the effect will depend on how depleted the anion concentration is.

Because the space charge due to water ions is lowered in the depletion region, the bulk liquid in a system with a wide depletion region can carry a smaller cation current than the bulk in a system with thin depletion region. This effect can be so pronounced that the sum of the bulk and screening layer cation current, in a system with finite surface charge density, is smaller than the bulk cation current in the corresponding system with zero space charge density. Furthermore, as the generation of water ions in the depletion region increases with increased anion depletion more water ions will be generated in the system with zero surface charge density, and the current of water ions will thus be higher than in the system with finite surface charge. There are thus two related effects which can increase the current in the zero space charge case above the current in the finite space charge case. To illustrate this the current at a bias of $60\,\mathrm{V_T}$ is plotted for varying surface charge

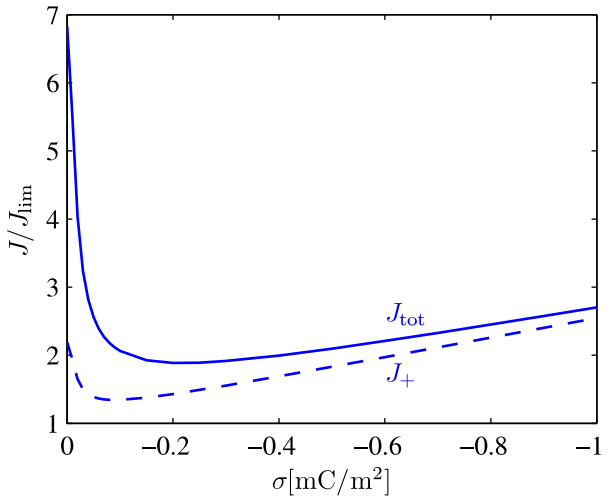

Figure 6.8: *Total current density (full line) and cation current density (dashed) plotted for a bias voltage of* $60\,V_T$ *versus the surface charge density. Parameters:* $c_0 = 1\,\text{mM}$, pH = 7, $L_{\text{ic}} = 1\,\text{mm}$, $L_{\text{m}} = 100\,\mu\text{m}$, $L_{\text{oc}} = 1\,\text{mm}$, $R = 1\,\mu\text{m}$.

densities in figure 6.8. A clear minimum is visible in the plot. For large surface charge densities surface conduction dominates the current which therefore increases linearly with the surface charge.

6.3.3 Dynamic surface charge density

In the study of the dynamic surface charge density the lengths $L_{\text{ic}} = 1\,\text{mm}$, $L_{\text{m}} = 100\,\mu\text{m}$ and $L_{\text{oc}} = 1\,\text{mm}$ were used again. The radius took on the values $R = 0.2\,\mu\text{m}$, $R = 1\,\mu\text{m}$ and $R = 5\,\mu\text{m}$, the reservoir salt concentration was varied from $c_0 = 0.1\,\text{mM}$ over $c_0 = 1\,\text{mM}$ to $c_0 = 10\,\text{mM}$ and the reservoir pH took on the values 5.5, 7 and 8.5.

Before presenting the I-V curves we will consider the effect of the concentration fields on the surface charge density. In figure 6.9 the surface charge density is plotted versus the bulk ionic strength (assuming electroneutrality) and the bulk pH for a channel of radius $R = 5\,\mu\text{m}$[1]. As predicted in section 4.3 the magnitude of the surface charge density increases with both pH and ionic strength.

Because of the dynamic surface charge density the amount of ions which can be conducted through the screening layers depends on the bulk hydronium and salt concentration. This influence is evident in the I-V curves, where the overlimiting conductance varies significantly with the bias voltage. In figure 6.10 the total current density is plotted in a channel of radius $R = 1\,\mu\text{m}$ for varying c_0 and pH, and in figure 6.10 the current is plotted in a channel of radius $R = 5\,\mu\text{m}$. The currents are normalised with the limiting current, so in fact the current is smaller for $c_0 = 1\,\text{mM}$ than for $c_0 = 10\,\text{mM}$ although the plots seem to show the opposite. The average current densities are larger for small radii

[1]Because the width of the screening layers is much smaller than the radius, the radius will have a negligible influence on the surface charge density.

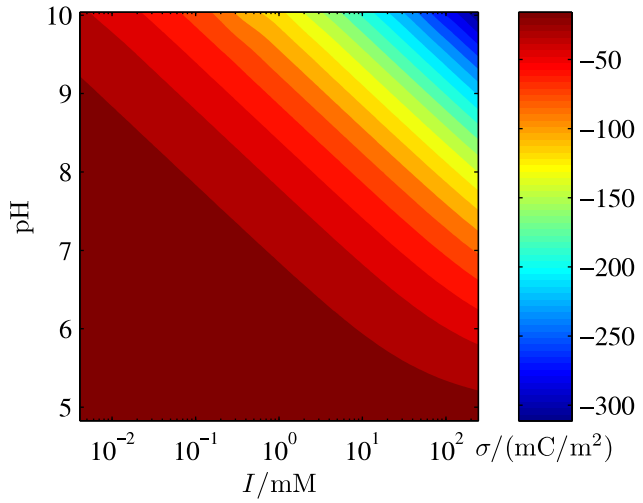

Figure 6.9: *The surface charge density in a microchannel of radius $R = 5\,\mu$m plotted as function of the bulk pH and the bulk ionic strength. The magnitude of the surface charge density is seen to increase monotonically with both parameters.*

(figure 6.10) than for large radii (figure 6.11) because surface conduction is relatively more important when the channel circumference to cross-section ratio is large. For both radii there is seen to be roughly three distinct regimes (most visible for $R = 5\,\mu$m): A regime below the limiting current where a large portion of the current is carried in the bulk, and two overlimiting regimes each with their own differential conductance.

We can rationalise the two overlimiting regimes using some of the arguments from section 6.3.2. The overlimiting regime starts when the salt concentration at the membrane has decreased to roughly a hundredth of the inlet concentration. The concentration in the depletion region will continue to drop as the voltage is increased above the limiting value, but this has a negligible effect on the bulk current because the conductivity scales linearly with the salt concentration. The surface charge density does however have an approximately logarithmic dependence on the salt concentration, making the continued depletion of salt ions important. To show the logarithmic dependence we consider the approximate expression from equation (4.25) in the high ζ limit

$$\sigma \approx -3C_\mathrm{s}V_\mathrm{T}\mathrm{W}\left(\frac{\frac{\epsilon_\mathrm{w}}{\lambda_\mathrm{D}}}{3C_\mathrm{s}}\left[\frac{e\Gamma K_\mathrm{SiOH}}{c_\mathrm{H,bulk}V_\mathrm{T}\frac{\epsilon_\mathrm{w}}{\lambda_\mathrm{D}}}\right]^{1/3}\right) \tag{6.27}$$

$$\approx -\left(V_\mathrm{T}\frac{\epsilon_\mathrm{w}}{\lambda_\mathrm{D,0}}\right)^{2/3}\left(\frac{e\Gamma K_\mathrm{SiOH}}{\sqrt{K_\mathrm{w}}}\right)^{1/3}\left[\frac{1}{3}\left(\breve{c}_+ - \breve{c}_\mathrm{H}\right) - \ln\left(\frac{1}{3}\left(\breve{c}_+ - \breve{c}_\mathrm{H}\right)\right)\right], \tag{6.28}$$

where $\lambda_\mathrm{D,0}$ is the Debye length evaluated for the inlet concentration c_0, and we have introduced the logarithmic concentration fields

$$\breve{c}_\pm = \ln\left(\frac{c_\pm}{c_0}\right) \quad \text{and} \quad \breve{c}_\mathrm{H} = \ln\left(\frac{c_\mathrm{H}}{\sqrt{K_\mathrm{w}}}\right). \tag{6.29}$$

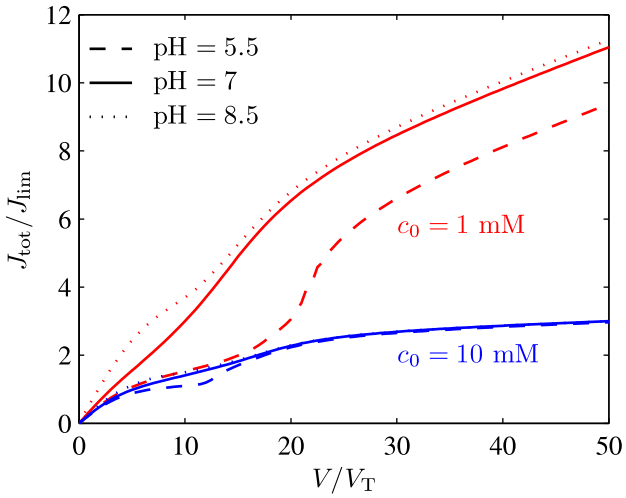

Figure 6.10: *Average current densities for model with dynamic surface charge and* $R = 1\,\mu$m. *Parameters:* $L_{\text{ic}} = 1\,$mm, $L_{\text{m}} = 100\,\mu$m, $L_{\text{oc}} = 1\,$mm.

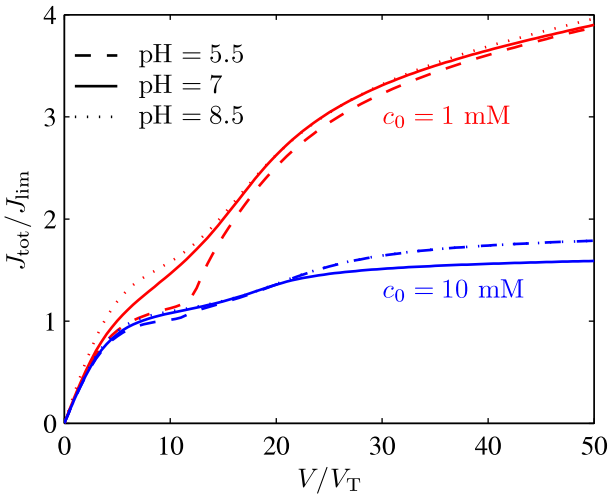

Figure 6.11: *Average current densities for model with dynamic surface charge and* $R = 5\,\mu$m. *Parameters:* $L_{\text{ic}} = 1\,$mm, $L_{\text{m}} = 100\,\mu$m, $L_{\text{oc}} = 1\,$mm.

The magnitude of the surface charge density thus decreases as the salt concentration continues its depletion, and since the amount of surface current depends on the surface charge density this will greatly affect the overlimiting current.

At a certain voltage the depletion of the salt concentration stops and the depletion region starts expanding instead. There is thus a lower limit to the magnitude of the surface charge density and this is the reason for the systems largely constant differential conductance at high voltages.

In figure 6.12 and 6.13 the axial cation concentration and the surface charge density are plotted for a system with $R = 5\,\mu$m, $c_0 = 1\,$mM and pH = 7. At high voltages the surface charge density is seen to approach a limiting value in the depletion region.

A feature shared by the current voltage curves in figure 6.10 and 6.11 is that for low voltages the curve for pH = 5.5 lies below the curve for pH = 7 and the curve for pH = 8.5 lies above. The reason for this is that the magnitude of the surface charge density increases with pH.

For high voltages the concentration of water ions in most of the channel is driven far away from the inlet concentration, and it follows that all three pH curves should nearly collapse. There are seen to be some exceptions from this rule. One is the $c_0 = 1\,$mM, pH = 5.5 curve in figure 6.10, which remains at a significantly lower value than its pH = 7 and pH = 8.5 counterparts. We earlier argued that the amount of water ion generation decreases with the relative importance of surface conduction. Surface conduction plays the largest role in thin channels for low concentrations, so the reason why all three $c_0 = 1\,$mM curves in figure 6.10 do not collapse is that the amount of water ion generation is

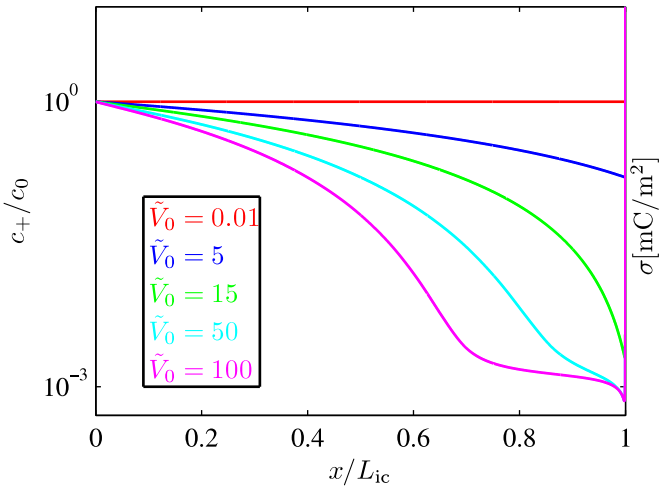

Figure 6.12: *Axial cation concentration in a model with dynamic surface charge and* $R = 5\,\mu$m. *Parameters:* $c_0 = 1\,$mM, pH $= 7$, $L_{\mathrm{ic}} = 1\,$mm, $L_{\mathrm{m}} = 100\,\mu$m, $L_{\mathrm{oc}} = 1\,$mm.

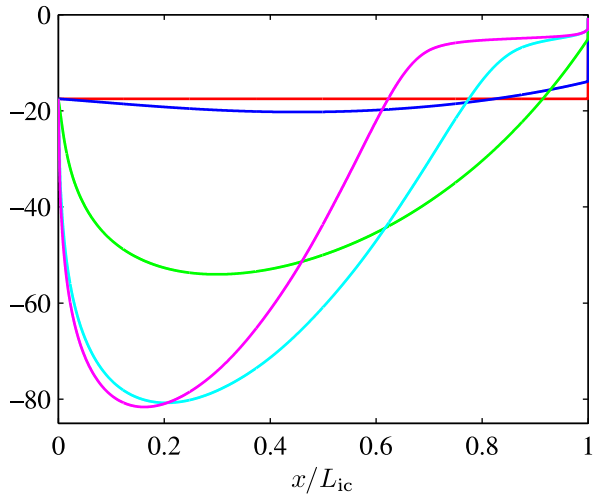

Figure 6.13: *Dynamic surface charge density in a model with* $R = 5\,\mu$m. *Parameters:* $c_0 = 1\,$mM, pH $= 7$, $L_{\mathrm{ic}} = 1\,$mm, $L_{\mathrm{m}} = 100\,\mu$m, $L_{\mathrm{oc}} = 1\,$mm.

insufficient for a decoupling of bulk and inlet pH.

In the $c_0 = 10\,$mM curve in figure 6.11 surface conduction is relatively less important and more water ion generation is thus expected. It follows that a significant part of the total current will be from water ions. The fact that the pH $= 5.5$ curve lies above the pH $= 7$ curve can then be explained by the higher inlet concentration of hydronium, since this gives rise to a significant diffusive current into the depletion region.

For the same reason the pH $= 8.5$ curve would be expected to lie below the pH $= 7$ curve. This is however not the case. It is not entirely clear why the pH $= 8.5$ lies above the pH $= 7$ curve for $c_0 = 10\,$mM and $R = 5\,\mu$m, but it must have to do with the dynamic surface charge since the same phenomenon is not observed when carrying out a simulation with fixed surface charge density.

The results found for $R = 0.2\,\mu$m and $c_0 = 0.1\,$mM are in agreement with the arguments given above. We have however chosen not to show them here as they are heavily dominated by surface conduction and thus makes for poor plotting material.

The extent of the depletion region depends on the inlet concentration of salt ions. To illustrate this, the cation concentration has been plotted in figure 6.14 for three different inlet concentrations and a bias voltage of $V_0 = 100V_{\mathrm{T}}$. The radius in the channel is $R = 1\,\mu$m. The extent of the depletion region decreases with increasing inlet concentration. This is not surprising since a high concentration means that surface conduction is relatively less important, and we have already seen that in the limit of vanishing surface conduction the depletion region is very thin. Interestingly, the concentration in the depletion region is seen to be independent of the inlet concentration.

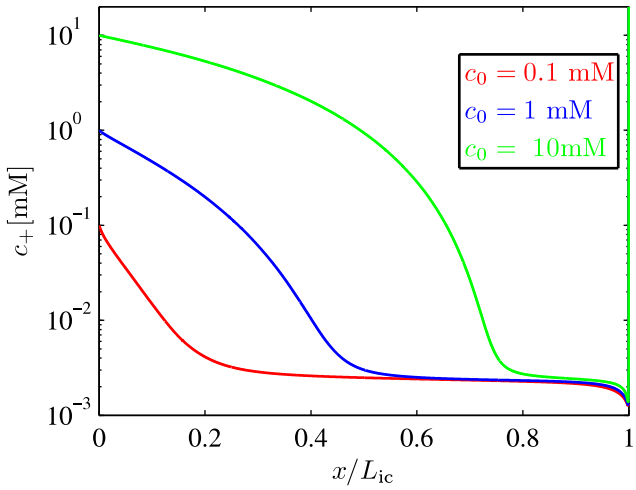

Figure 6.14: *The axial cation concentration plotted in a channel of radius* $R = 1\,\mu$m *for different inlet concentrations. The extent of the depletion zone is seen to vary with the inlet concentration, while the concentration in the depletion region is nearly independent of the inlet concentration. Parameters:* $V_0 = 100V_{\mathrm{T}}$, pH $= 7$, $L_{\mathrm{ic}} = 1\,$mm, $L_{\mathrm{m}} = 100\,\mu$m, $L_{\mathrm{oc}} = 1\,$mm.

To conclude on this chapter we have shown the existence of an extra overlimiting regime for ion transport in microchannels containing an ion-selective membrane. We have rationalised the behaviour of the system and argued that it is a function of complex couplings between ion transport, bulk and surface reactions and the ion-selective membrane. Furthermore, we have found a non-monotonic dependence of the current density as a function of the wall surface charge. We have explained that this is the result of reduced water splitting in systems where surface conduction is important.

Chapter 7

Axisymmetric 3D model

Although the 1D models used in the previous chapter can give valuable insight in some of the fundamental physical phenomena, they fall short near the membrane and in wide channels. To accurately model these cases a 2D/axisymmetric 3D model[1] is required.

7.1 Implementation of the 2D model

The governing equations (2.3), (2.6), (2.9) and (2.12) in cylindrical coordinates are written in weak form and put into Comsol along with the appropriate boundary conditions. On all walls and the membrane a no slip boundary condition is imposed on the velocity field. At the inlet the radial velocity field is set to zero and so is the axial derivative of the axial velocity.

Because the important physics happens in the left channel, the entirety of the right channel can be modelled using the 1D model with only negligible effect on the obtained results. Likewise, the membrane region is well-described using a 1D model. In this way only the left channel has to be modelled using a full 2D model.

A major challenge when implementing the 2D problem is the meshing of the domain. If we were to resolve the boundary layers of characteristic length $\sim 0.1\,\mathrm{nm}$ using triangular mesh elements an immense amount of mesh elements would be needed. Instead we use so-called boundary layer elements which are long and very thin rectangular elements. From the geometry of these elements it follows that they will offer excellent resolution in one direction and poor resolution in the other. Although the variation of the fields is greatest normal to the charged walls, there is also a significant variation in the tangential direction. For this reason we actually have to use a combination of mesh elements near the walls; an innermost layer composed of boundary layer elements resolving the steepest part the screening layer, and an outer layer composed of triangular mesh elements which resolves the slower varying part of the screening layer as wells as tangential variations. In the innermost layer there will in fact also be some tangential variation, but we have to ignore

[1] We will most often refer to this model as a 2D model.

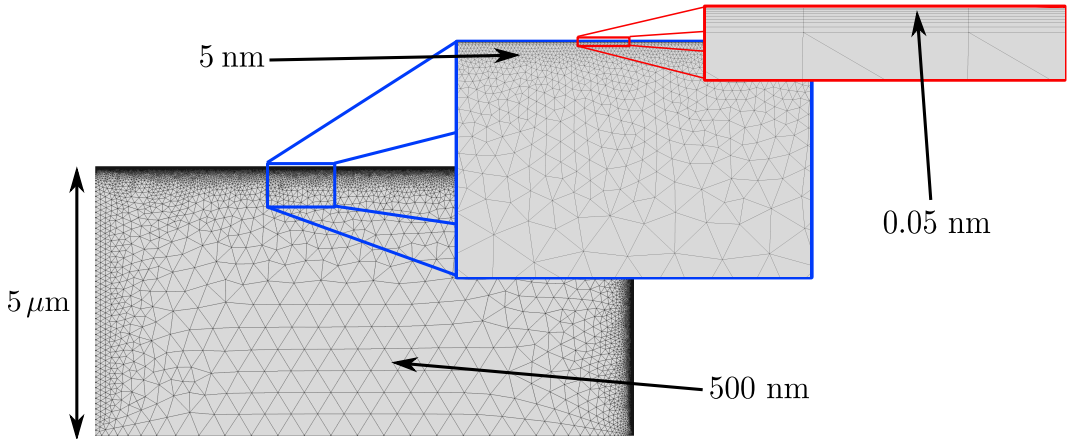

Figure 7.1: *Meshing of the 2D domain shown for a channel of radius $R = 5\,\mu$m. To resolve the innermost part of the screening layer a rectangular boundary layer is used, while the outer part of the screening layer is resolved using a triangular mesh. The size of the mesh elements is marked at different points.*

that to get a treatable number of mesh elements. In figure 7.1 the mesh is shown for the case of a channel of radius $R = 5\,\mu$m.

7.2 Results

From equation (6.19) we know that the 1D model will break down for large radii R. To test what happens in that limit we carry out a 2D simulation of a system with radius $R = 5\,\mu$m and $L_{\text{ic}} = 10\,\mu$m, $L_{\text{m}} = 100\,\mu$m, $L_{\text{oc}} = 100\,\mu$m, $c_0 = 1\,$mM, pH = 7. The resulting current voltage relationship is shown in figure 7.2 (red). Comparing to the corresponding curve obtained for the 1D model (figure 6.11)[2] we see that they are very different. In the 1D model there are two very pronounced overlimiting regimes whereas the curve for the 2D model only bends slightly at the limiting current. The main reason for this discrepancy is the influence of advection. To show that we have carried out the same 2D simulation once more, only this time without including fluid flow in the model. The resulting I-V curve is shown in figure 7.2 (blue) and it is seen to qualitatively resemble the curve found in the 1D model.

The case with fluid flow is radically different because the region in front of the membrane is advectively mixed, and this prevents the build up of a depletion region. In figure 7.3 the cation concentration in the channel is shown together with arrows illustrating the velocity field for a bias voltage of $V_0 = 40V_{\text{T}}$. The cation concentration is seen to be much larger in the outer half of the channel than in the inner half, because liquid of high concentration flows towards the membrane along the edge and liquid of low concentration flows backwards in the centre. A requirement for this to happen is that the axial convective

[2] A larger length of the inlet channel was used in that simulation, but it still makes sense to make a qualitative comparison.

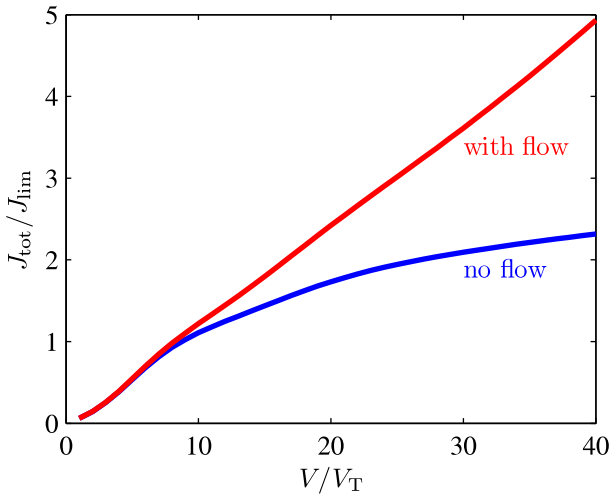

Figure 7.2: *I-V curves for a 2D model with dynamic surface charge and* $R = 5\,\mu$m*. The curve for the model including advection is seen to be radically different from the curve for the model without advection. Parameters:* $c_0 = 1\,$mM, pH $= 7$, $L_{\mathrm{ic}} = 10\,\mu$m, $L_{\mathrm{m}} = 100\,\mu$m, $L_{\mathrm{oc}} = 100\,\mu$m.

transport is considerably faster than the radial transport, i.e.

$$\frac{L_0}{u_0} < \frac{R^2}{D}, \tag{7.1}$$

where the characteristic velocity for electroosmotic flow is the Helmholtz-Smoluchowski velocity given as

$$u_0 = \frac{\zeta \epsilon_{\mathrm{w}}}{\eta} E. \tag{7.2}$$

Due to the R^2 dependence of the radial transport time the transition between the regimes where advective mixing is important and unimportant will be rather abrupt when varying the radius.

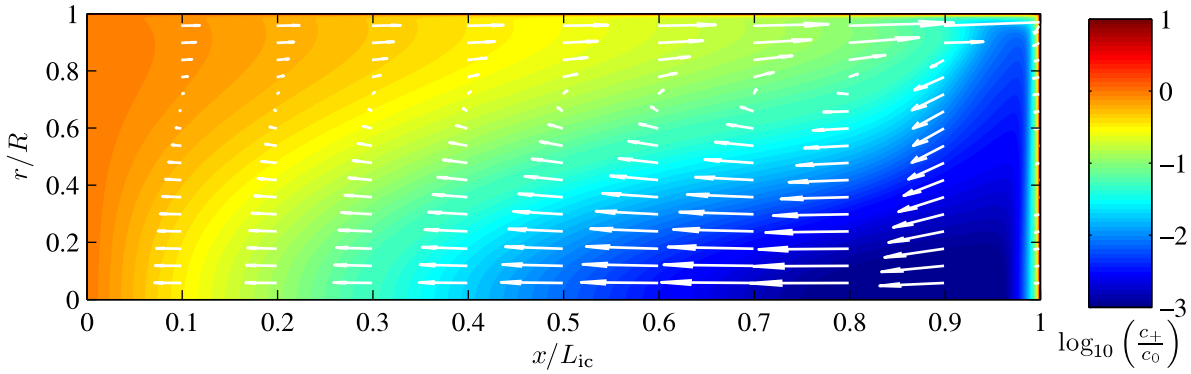

Figure 7.3: *Cation concentration (color) and velocity field (arrows) for a 2D model with dynamic surface charge and* $R = 5\,\mu\text{m}$. *It is seen that the concentration field is out of equilibrium in the radial direction. Parameters:* $c_0 = 1\,\text{mM}$, pH = 7, $L_{\text{ic}} = 10\,\mu\text{m}$, $L_{\text{m}} = 100\,\mu\text{m}$, $L_{\text{oc}} = 100\,\mu\text{m}$.

Chapter 8

A coupled 1D-2D model for the ion transport

The computational cost of running a 2D simulation makes it inconvenient to simulate large systems using a full 2D model. On the other hand the 1D model does not fully describe the physics close to the membrane. For channels which are not too wide the 1D model does however give a good description of the region far away from the membrane. We will therefore attempt to combine the accuracy of the 2D model with the low computational cost of the 1D model by modelling the part of the system far from the membrane using the 1D model, and the part of the system close to the membrane using a 2D model.

8.1 Coupling of 1D and 2D model

The 1D model is valid when the inequality (6.19) is satisfied, and from this it follows that the domain of validity will depend on the extent of the depletion zone. During a voltage sweep the depletion zone expands and the point where 1D and 2D model couples should thus be able to move. In Comsol this means that the 1D domain should shrink and the 2D domain should expand. While it is possible to sweep over geometries in Comsol, it makes it impossible to use the previous solution as a starting guess because the remeshing of the domains introduces a new FEM basis. Due to the nonlinearity of the problem, solutions for high bias voltages require a good starting guess, i.e. it requires that the previous solution is used as an initial condition.

We can get around this problem by scaling the spatial variables to effectively change the domain size without having to change the geometry. Stretching the 2D domain using scaling variables has the effect of effectively coarsening the mesh. This could be problematic, but conveniently the relevant physical length scale (the Debye length) expands at the same time as the mesh is coarsened, because the salt concentration in the depletion region becomes very low.

The inlet channel of length L_{ic} is divided into an inlet region of length L_{ir}, modelled

using the 1D model, and a transition region of length L_{tr}, modelled using the 2D model. We also introduce the unscaled lengths of the regions $L_{\text{ir},0}$ and $L_{\text{tr},0}$. The spatial variable in the axial direction x can be related to the unscaled variable $\hat{x}$ as

$$x = \frac{L_{\text{ir}}}{L_{\text{ir},0}}\hat{x} \quad \text{In the inlet region,} \tag{8.1a}$$

$$x = L_{\text{ir}} + \frac{L_{\text{tr}}}{L_{\text{tr},0}}\hat{x} \quad \text{In the transition region.} \tag{8.1b}$$

It proves convenient to introduce the scaling parameters

$$\gamma_{\text{ir}} = \frac{L_{\text{ir}}}{L_{\text{ir},0}} \quad \text{and} \quad \gamma_{\text{tr}} = \frac{L_{\text{tr}}}{L_{\text{tr},0}}, \tag{8.2}$$

which are related as

$$\gamma_{\text{tr}} = 1 + \frac{L_{\text{ir},0}}{L_{\text{tr},0}}\left(1 - \gamma_{\text{ir}}\right), \tag{8.3}$$

since the total length of the channel is independent of the scaling. The derivatives then transform as

$$\frac{\partial}{\partial x} = \frac{1}{\gamma_\alpha}\frac{\partial}{\partial \hat{x}}, \tag{8.4}$$

where $\alpha \in \{\text{ir}, \text{tr}\}$.

Let us now consider how the scaling affects the governing equations and boundary conditions. To do that we consider the general PDE

$$\boldsymbol{\nabla} \cdot \boldsymbol{\Gamma} = F(\boldsymbol{x}), \tag{8.5}$$

which, as shown in section 5.1, can be rewritten in weak form

$$\int_{\partial\Omega} \psi_m \boldsymbol{n} \cdot \boldsymbol{\Gamma} \, \mathrm{d}\boldsymbol{x} + \int_\Omega -\boldsymbol{\nabla}\psi_m \cdot \boldsymbol{\Gamma} - \psi_m F(\boldsymbol{x}) \, \mathrm{d}\boldsymbol{x} = 0. \tag{8.6}$$

When scaled, any derivatives appearing in $\boldsymbol{\Gamma}$ and $F(\boldsymbol{x})$ should be modified according to (8.4). In a cylindrical geometry the volume integral becomes

$$\int_\Omega -\boldsymbol{\nabla}\psi_m \cdot \boldsymbol{\Gamma} - \psi_m F \, \mathrm{d}\boldsymbol{x} = \int_\Omega 2\pi r \left[-\partial_r \psi_m \Gamma_r - \partial_x \psi_m \Gamma_x - \psi_m F\right] \, \mathrm{d}r\mathrm{d}x \tag{8.7}$$

$$= \int_\Omega 2\pi r \left[-\partial_r \psi_m \Gamma_r - \frac{1}{\gamma_\alpha}\partial_{\hat{x}} \psi_m \Gamma_x - \psi_m F\right] \gamma_\alpha \, \mathrm{d}r\mathrm{d}\hat{x}, \tag{8.8}$$

and the surface integral becomes

$$\int_{\partial\Omega} \psi_m \boldsymbol{n} \cdot \boldsymbol{\Gamma} \, \mathrm{d}\boldsymbol{x} = \int_{\partial\Omega} 2\pi r \left[\psi_m n_x \Gamma_x + \psi_m \gamma_\alpha n_r \Gamma_r\right] \, \mathrm{d}r\mathrm{d}\hat{x}. \tag{8.9}$$

At the point where 1D and 2D model couples continuity of $\boldsymbol{\Gamma}$ and the dependent variables is required.

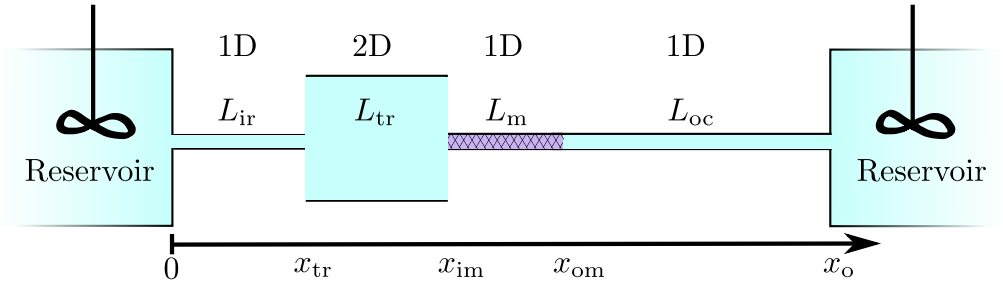

Figure 8.1: *Sketch of the model system illustrating which regions are being modelled using a 2D model and which regions are modelled using a 1D model.*

8.2 Implementation of the coupled 1D-2D model

As in the previous chapter we will model the membrane region and the right channel using a 1D model. The system will thus be modelled as shown in figure 8.1, where also the position x_{tr} of the transition between 1D and 2D domain is introduced.

On the 1D side at x_{tr} we impose Neumann boundary conditions on the current densities and the electric field. The current densities are set to be equal to the average current densities at x_{tr} in the 2D domain. The electric field, i.e. minus the derivative of ϕ_{ax}, is set equal to the average electric field at x_{tr} in the 2D domain plus the average of the derivative of ϕ_{eq}.

$$\begin{aligned} \text{1D side} \qquad & & \text{2D side} & \\ J_i \quad &= \quad \langle \boldsymbol{n} \cdot \boldsymbol{J}_i \rangle \,, & & (8.10a) \\ \frac{1}{\gamma_{\mathrm{ir}}} \partial_{\hat{x}} \left\{ \phi_{\mathrm{ax}} + \langle \phi_{\mathrm{eq}} \rangle \right\} \quad &= \quad \frac{1}{\gamma_{\mathrm{tr}}} \langle \partial_{\hat{x}} \phi \rangle \,. & & (8.10b) \end{aligned}$$

On the 2D side at x_{tr} Dirichlet boundary conditions are used. The concentration fields and the potential are set equal to their counterpart in the 1D domain.

$$\begin{aligned} \text{2D side} \qquad & & \text{1D side} & \\ c_{\pm} \quad &= \quad k_{\pm} \mp \phi_{\mathrm{eq}}, & & (8.11a) \\ c_{\mathrm{H}} \quad &= \quad h - \phi_{\mathrm{eq}}, & & (8.11b) \\ \phi \quad &= \quad \phi_{\mathrm{ax}} + \phi_{\mathrm{eq}}. & & (8.11c) \end{aligned}$$

The equilibrium potential at x_{tr} is obtained by introducing an auxiliary 1D problem in which equation (6.5) is solved using the values of $k_{\pm}$ and h found at x_{tr}.

The Neumann boundary conditions only directly affect the 1D problem, because only basis functions from the 1D problem are present in the boundary term in the weak equation (5.9c). On the other hand the Dirichlet condition affects both the 1D and 2D problem through the constraint force (5.12), and this can make the joint problem appear overconstrained. To get around this issue we manually specify the constraint force so that it only includes basis functions from the 2D problem.

At the interface between the 2D domain and the membrane similar boundary conditions ensuring continuity of the relevant fields are implemented.

During a voltage sweep the location of x_{tr} should be changed continually, so that the 1D model is always valid. According to (6.19) the position of x_{tr} should be based on considerations about the logarithmic derivative of a representative concentration field. Instead we will however use the concentration itself as a criteria for changing the position of x_{tr}, as this gives less ambiguity in the determination of x_{tr}. This criteria then defines x_{tr} in the following way: For a given voltage the value of x is found, for which the concentration takes on a predefined value. This value of x is then used as x_{tr} for the next bias voltage in the sweep.

Because Comsol does not support data processing during a sweep it is rather cumbersome to implement this method of moving x_{tr}. It can however be done by introducing several additional solver steps, some new domains and an inverter function.

8.3 Results

We are primarily interested in simulating systems with $R = 0.6\,\mu\mathrm{m}$ as the microchannels found in the system shown in figure 3.1 are of roughly that size. To validate the coupled 1D-2D model in the case of $R = 0.6\,\mu\mathrm{m}$ two simulations with $L_{\mathrm{ic}} = 30\,\mu\mathrm{m}$ have been carried out. In one simulation the entire inlet channel was modelled using a 2D model and in the other simulation the inlet channel was modelled using the 1D-2D model with the initial lengths $L_{\mathrm{ir},0} = 20\,\mu\mathrm{m}$ and $L_{\mathrm{tr},0} = 10\,\mu\mathrm{m}$. Both simulations used $L_{\mathrm{m}} = 100\,\mu\mathrm{m}$, $L_{\mathrm{oc}} = 100\,\mu\mathrm{m}$ and $\sigma = 1\,\mathrm{mC/m^2}$. In figure 8.2 the average total current density is plotted as a function of bias voltage for the two simulations, and in figure 8.3 the axial cation concentration in the inlet channel is plotted for 4 different bias voltages. In both plots there is seen to be excellent agreement between the two models. To further document the agreement between the two models the velocity fields have been plotted for $V_0 = 30V_{\mathrm{T}}$ in figure 8.4. For the 1D-2D model we can naturally only plot the velocity in the transition region, but in this region the models are seen to agree nicely.

Having established that the 1D-2D model accurately describes the physics in a thin microchannel, we will apply it to a much longer channel with dynamic surface charge density. The length of the inlet channel is set to $L_{\mathrm{ic}} = 100\,\mu\mathrm{m}$ divided into an inlet region of initial length $L_{\mathrm{ir},0} = 90\,\mu\mathrm{m}$ and a transition region of length $L_{\mathrm{tr},0} = 10\,\mu\mathrm{m}$. Again, we choose $R = 0.6\,\mu\mathrm{m}$, $L_{\mathrm{m}} = 100\,\mu\mathrm{m}$ and $L_{\mathrm{oc}} = 100\,\mu\mathrm{m}$. In figure 8.5 the current is plotted versus the bias voltage. For a channel this thin the surface current is large relative to the bulk current, and for this reason there is no visible bending of the curve at the limiting current. For large voltages the differential conductance falls to a lower and nearly constant value due to the constant low surface charge density in the depletion region. In figure 8.6 the cation concentration and the surface charge density are plotted for four values of the bias voltage. The position of the coupling between 1D and 2D model is marked with a black circle.

The curve in figure 8.5 is our best bid at how the current-voltage curve for the system

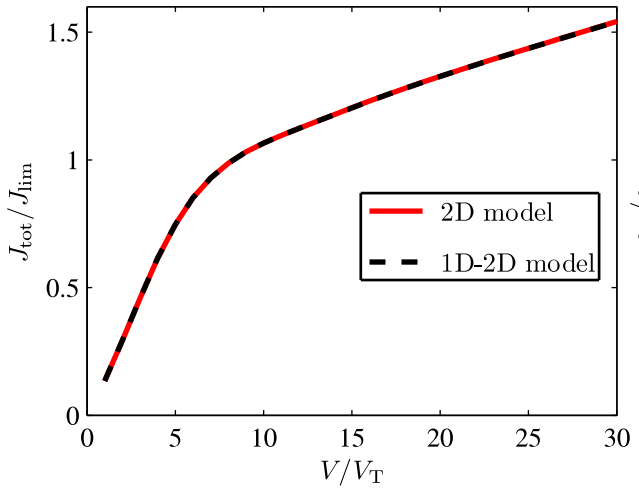

Figure 8.2: *Average current density in a system with* $\sigma = 1\,\mathrm{mC/m^2}$ *for two different models. In one model the entire inlet channel is modelled as a 2D domain and in the other model part of the inlet channel is modelled as 1D. The two models are seen to agree excellently. Parameters:* $c_0 = 1\,\mathrm{mC/m^2}$, pH $= 7$, $L_{\rm ic} = 30\,\mu$m, $L_{\rm ir,0} = 20\,\mu$m, $L_{\rm tr,0} = 10\,\mu$m, $L_{\rm m} = 100\,\mu$m, $L_{\rm oc} = 100\,\mu$m.

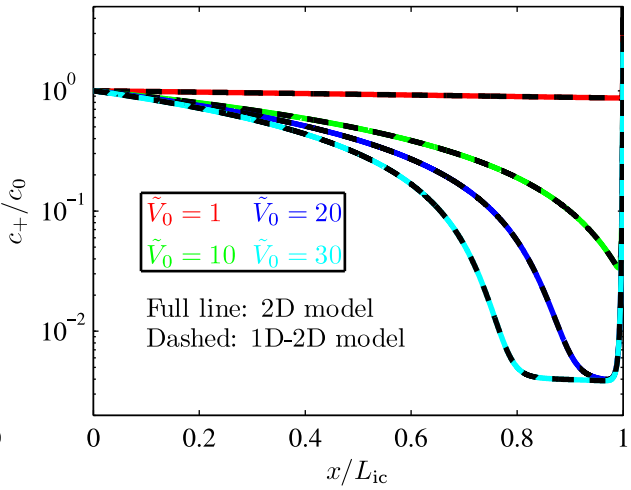

Figure 8.3: *Cation concentration in the inlet channel in a system with* $\sigma = 1\,\mathrm{mC/m^2}$ *for two different models. In one model the entire inlet channel is modelled as a 2D domain and in the other model part of the inlet channel is modelled as 1D. The two models are seen to agree excellently. Parameters:* $c_0 = 1\,\mathrm{mC/m^2}$, pH $= 7$, $L_{\rm ic} = 30\,\mu$m, $L_{\rm ir,0} = 20\,\mu$m, $L_{\rm tr,0} = 10\,\mu$m, $L_{\rm m} = 100\,\mu$m, $L_{\rm oc} = 100\,\mu$m.

in figure 3.1 will look (with a rescaling of the axis due to the longer channel length). It should however be noted that the appearance of the curve is quite sensitive to the values of the surface reaction constants and the surface site density.

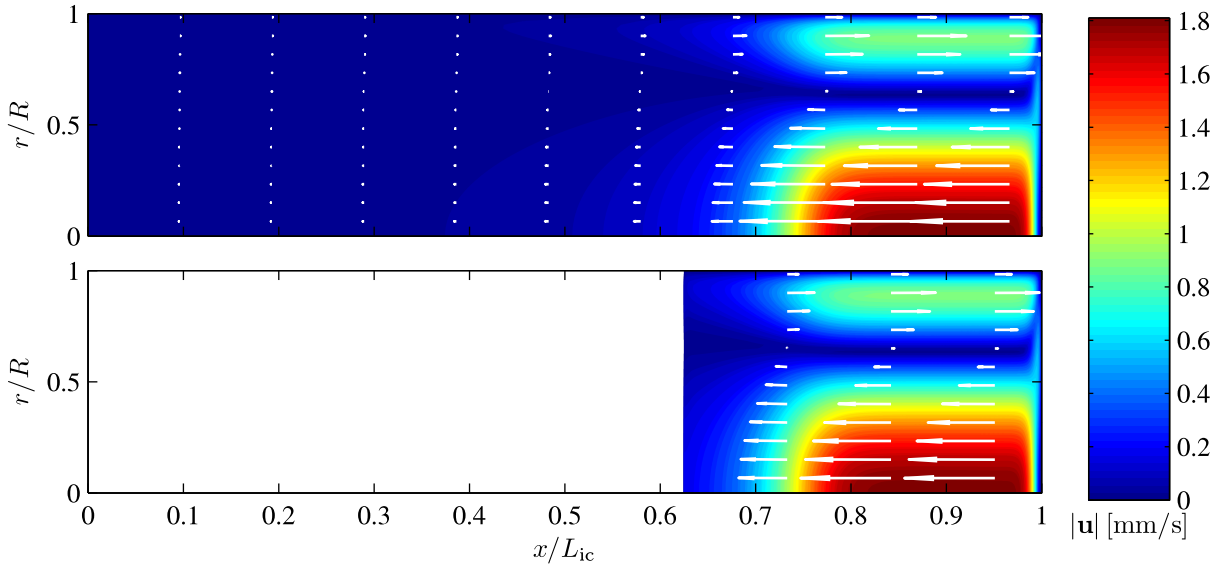

Figure 8.4: *Velocity fields in the inlet channel in a system with* $\sigma = 1\,\mathrm{mC/m^2}$ *for two different models. In one model the entire inlet channel is modelled as a 2D domain and in the other model part of the inlet channel is modelled as 1D. The colors show the magnitude of the velocity and the white arrows show the direction of the flow. In the transition region both models are seen agree nicely. Parameters:* $c_0 = 1\,\mathrm{mC/m^2}$, pH $= 7$, $L_\mathrm{ic} = 30\,\mu\mathrm{m}$, $L_\mathrm{ir,0} = 20\,\mu\mathrm{m}$, $L_\mathrm{tr,0} = 10\,\mu\mathrm{m}$, $L_\mathrm{m} = 100\,\mu\mathrm{m}$, $L_\mathrm{oc} = 100\,\mu\mathrm{m}$.

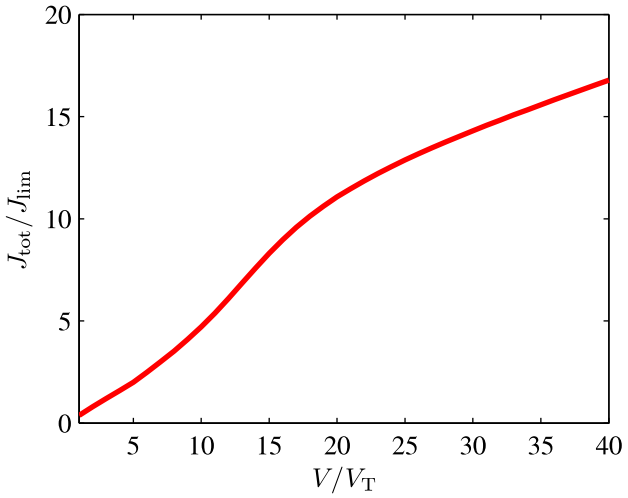

Figure 8.5: *I-V curve for a 1D-2D model of a channel with dynamic surface charge and* $R = 0.6\,\mu\mathrm{m}$. *Parameters:* $c_0 = 1\,\mathrm{mC/m^2}$, pH $= 7$, $L_\mathrm{ic} = 100\,\mu\mathrm{m}$, $L_\mathrm{ir,0} = 90\,\mu\mathrm{m}$, $L_\mathrm{tr,0} = 10\,\mu\mathrm{m}$, $L_\mathrm{m} = 100\,\mu\mathrm{m}$, $L_\mathrm{oc} = 100\,\mu\mathrm{m}$.

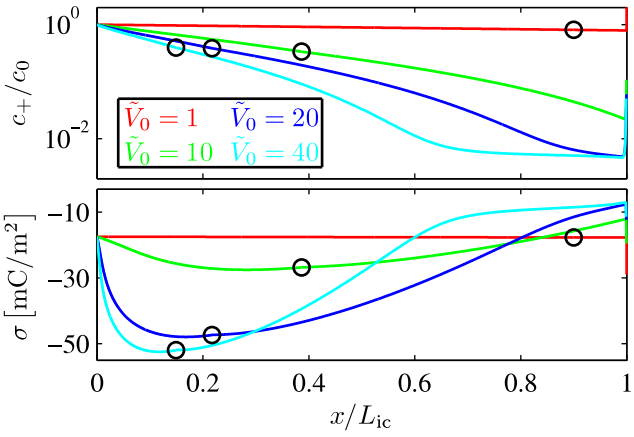

Figure 8.6: *Axial cation concentration for a 1D-2D model of a channel with dynamic surface charge and* $R = 0.6\,\mu\mathrm{m}$. *Parameters:* $c_0 = 1\,\mathrm{mC/m^2}$, pH $= 7$, $L_\mathrm{ic} = 100\,\mu\mathrm{m}$, $L_\mathrm{ir,0} = 90\,\mu\mathrm{m}$, $L_\mathrm{tr,0} = 10\,\mu\mathrm{m}$, $L_\mathrm{m} = 100\,\mu\mathrm{m}$, $L_\mathrm{oc} = 100\,\mu\mathrm{m}$.

Chapter 9

Desalination device

One of the envisioned applications of the system constructed in the group of Martin Bazant (figure 3.1) is as a desalination device. In this chapter we will construct a simple model of such a desalination device and simulate the operation of it. The basic idea in this type of desalination device is to flush out the ion-depleted water in the depletion region. Using the physical insight obtained in the previous chapters, we can already at this point say something about which physical effects will be important for the operation of such a device.

Since the functioning of the device relies on the extended depletion zone it is important that such a zone exists. In chapter 6 we argued that the extent of the depletion zone depends on the relative importance of surface conduction, so to get a sufficiently extended depletion zone some combination of low salt concentration, high surface charge density and narrow channels should be used.

In chapter 7 we found that advective mixing could greatly change the overlimiting behaviour of a system. In figure 7.3 it is seen that advection carries high concentration liquid towards the membrane along the edge of the channel. Since the desalination device would function by flushing water out through a side channel this is a highly undesirable effect. To minimise this effect the radial transport should be considerably faster than the axial convective transport, i.e.

$$\frac{R^2}{D} \ll \frac{L_0}{u_0}. \tag{9.1}$$

The left hand side is strongly R dependent, so a straight-forward way of minimising the left hand side is to reduce R. This also acts to make surface conduction relatively more important.

The simplest design of a system, where the liquid near the membrane can be flushed out, is a long straight channel with an ion-selective membrane in the middle and a side channel just to the left of the membrane. A sketch of such a system is shown in figure 9.1.

There is a potentially large number of factors affecting the performance of this desalination device, and it would be a daunting task to investigate the effect of them all. We

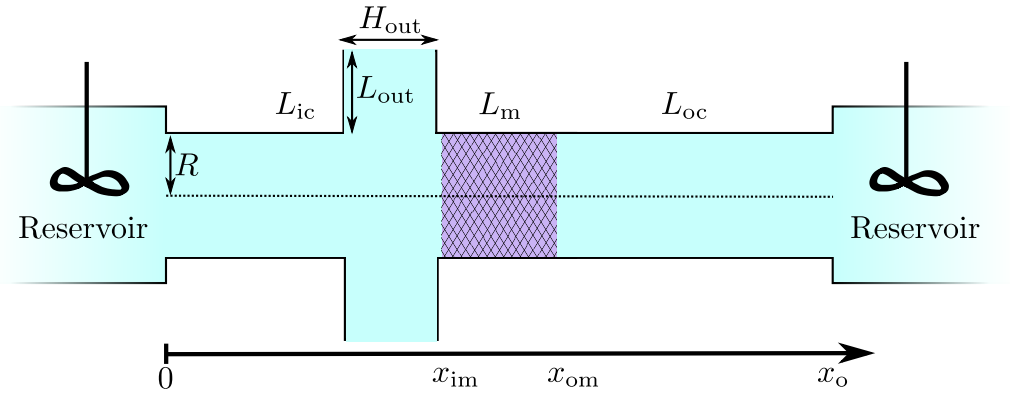

Figure 9.1: *Model of a desalination device.*

therefore fix the radius at $R = 0.6\,\mu$m and the lengths at $L_{\text{ic}} = 20\,\mu$m, $L_{\text{m}} = 100\,\mu$m, $L_{\text{oc}} = 100\,\mu$m, $L_{\text{out}} = R$ and $H_{\text{out}} = R$.

To transport liquid out of the system a net flow rate is needed. It is however clear that the higher the flow from inlet reservoir to the side channel, the more salt will be transported towards the membrane. This will decrease the amount of depletion and thus increase the concentration of the liquid being flushed out. A compromise therefore has to be found between the need for a low concentration in the flushed out liquid and a high flow rate.

Initially, we do however only want to investigate if the flushed out liquid can get sufficiently desalinated. As the depletion is maximised for zero flow rate we will limit ourselves to an investigation of that case as a start.

9.1 Implementation

In the left channel we implement boundary conditions and governing equations as done in chapter 7. Also, the mesh is constructed in roughly the same way. The corners where the inlet channel and side channel connects are rounded to avoid spurious edge effects. Again we model the membrane region and the right channel using the 1D model.

At the side channel outlet we require the normal derivatives of the concentration fields and the potential to vanish, implying purely convective transport of the salt ions. The tangential component of the velocity field and the normal derivative of the normal component are both set to zero at the outlet.

The net flow rate in the system is controlled by electroosmosis and the pressure difference between inlet reservoir and side channel. It is inconvenient to control the flow using electroosmosis as it is a function of the other system parameters $c_{\pm}$, σ and ϕ. The pressure difference is however easy to control independently of the other system parameters. To make sure that the pressure difference always has the value which will make the net flow rate zero we let it be a dependent variable and introduce an extra equation in the problem.

The extra equation simply states that the flow rate at the inlet reservoir is zero

$$\langle \boldsymbol{n} \cdot \boldsymbol{u} \rangle = 0, \quad \text{At the inlet reservoir,} \tag{9.2}$$

and the pressure difference is then adapted so that this equation is fulfilled.

9.2 Results

We begin our investigations with simulating a system with $c_0 = 1\,\text{mM}$. As the bias voltage is increased the average salt concentration at the outlet of the side channel is recorded. The resulting voltage-concentration plot is seen in figure 9.2. There is clearly seen to be an optimum at a bias voltage of $20V_\text{T}$.

For none of the systems we have previously investigated did a higher bias voltage lead to a less pronounced depletion in front of the membrane. In figure 9.3 it is seen that also the axial cation concentration behaves radically different from the systems we have hitherto studied.

The reason for these differences is that the pathway for surface conduction is effectively cut over by the outlet channel, so that the rightmost part of the inlet channel resembles a system without surface charge density. To illustrate how the minimum in figure 9.2 comes about the cation concentration in the channel has been plotted in figure 9.4 for the optimum voltage $V_0 = 20V_\text{T}$ and the much higher voltage $V_0 = 300V_\text{T}$. It is seen that at high voltages the concentration in the side channel is considerably larger than in the inlet channel. The reason for this is that the ions being conducted in the screening layers follow the wall up into the side channel, and they then cross over the side channel to the screening layer on the other side. This effect is clearly seen in figure 9.5, where the magnitude of the cation current density is plotted in the channel.

Let us return to the plot in figure 9.2. Even at the optimum bias voltage the anion and cation concentrations at the side channel outlet are only decreased to 2% and 4% of the inlet concentration, and the decrease is expected to be even lower when there is a net flow rate in the channel. This is hardly an impressive performance. From the discussion in chapter 6 we do however know that the concentration in the depletion region will be largely independent of the inlet concentration. Since seawater has a much higher salt concentration ($\sim 600\,\text{mM}$) than the considered inlet reservoir, we may thus be able to get a higher fractional concentration decrease when using sea water than when using water of salt concentration 1 mM. To test that we carry out a simulation with an inlet concentration of 600 mM and plot the average concentration at the side channel outlet versus bias voltage. The plot is seen in figure 9.6. In this plot there is seen to be a minimum at $V_0 = 140V_\text{T}$, but the minimum is a lot less pronounced than for the lower salt concentration. We also note that at the minimum the concentration is a lot higher (3.4 mM) than for the case of 1 mM inlet concentration, even though we would expect comparable concentrations in the depletion region.

The reason for the relatively high outlet concentration is that the high salt concentration in seawater is comparable to the concentration of charges in the ion-selective mem-

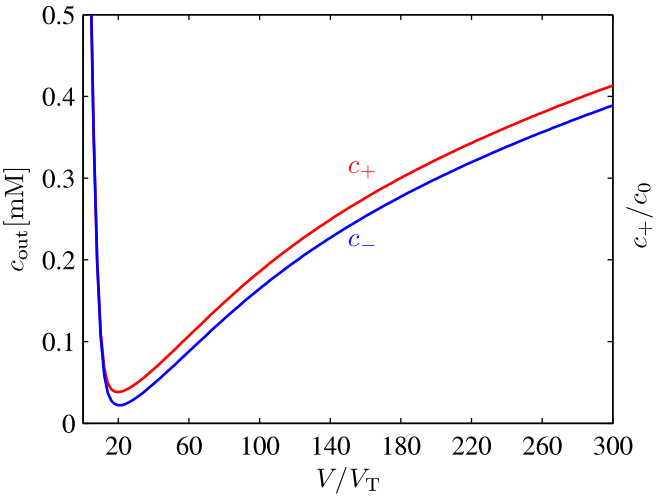

Figure 9.2: *Salt concentration at the side channel outlet for* $c_0 = 1\,\text{mM}$. *There is seen to be a minimum for* $V_0 = 20V_{\text{T}}$. *Parameters:* pH $= 7$, $R = 0.6\,\mu\text{m}$, $L_{\text{ic}} = 20\,\mu\text{m}$, $L_{\text{m}} = 100\,\mu\text{m}$, $L_{\text{oc}} = 100\,\mu\text{m}$, $L_{\text{out}} = R$, $H_{\text{out}} = R$.

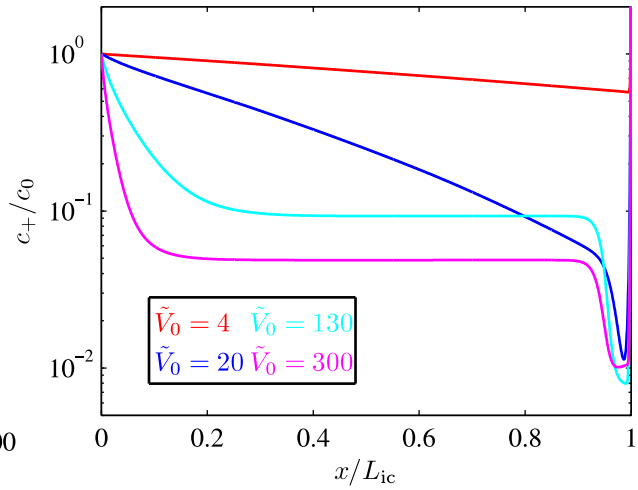

Figure 9.3: *Axial cation concentration in a desalination device for* $c_0 = 1\,\text{mM}$. *For high voltages there is seen to be two depletion regions. A narrow region close to the membrane where the concentration is heavily depleted, and a much wider region extending into the channel where the concentration has a constant and relatively high value. Parameters:* pH $= 7$, $R = 0.6\,\mu\text{m}$, $L_{\text{ic}} = 20\,\mu\text{m}$, $L_{\text{m}} = 100\,\mu\text{m}$, $L_{\text{oc}} = 100\,\mu\text{m}$, $L_{\text{out}} = R$, $H_{\text{out}} = R$.

brane. This causes the membrane to lose some of its selectivity and allow a considerable amount of anions to pass through. As a result the depletion region will be less pronounced than in the low concentration case.

The upper limit for salinity in drinking water is $\sim 8.7\,\text{mM}$ [30], so the water at the outlet is actually sufficiently desalinated for drinking purposes. Having established that the desalination device can yield sufficiently low outlet concentrations the next step is to assess how large a flow rate the device can function at. This task is complicated by the fact that the optimum bias voltage shift as the flow rate is increased. For each flow rate yet another voltage sweep would thus be required to find the operating point at that flow rate. While this certainly could be done it would require many days of calculations and it might not even be that relevant, since there is a critical problem with our model.

The reason for the minimum in figure 9.2 and 9.6 is that the cations cannot be conducted all the way to the membrane inside the screening layers but have to move through the bulk of the side channel. Let us compare that to the physical system we are attempting to model. In the system in figure 3.1 the void between the glass beads make up the microchannels leading up to the membrane. Because many of the glass beads touch there will be a whole grid of interlinked paths of surface conduction and no channel which cuts over all of them. In the physical system the cations will therefore not have to move

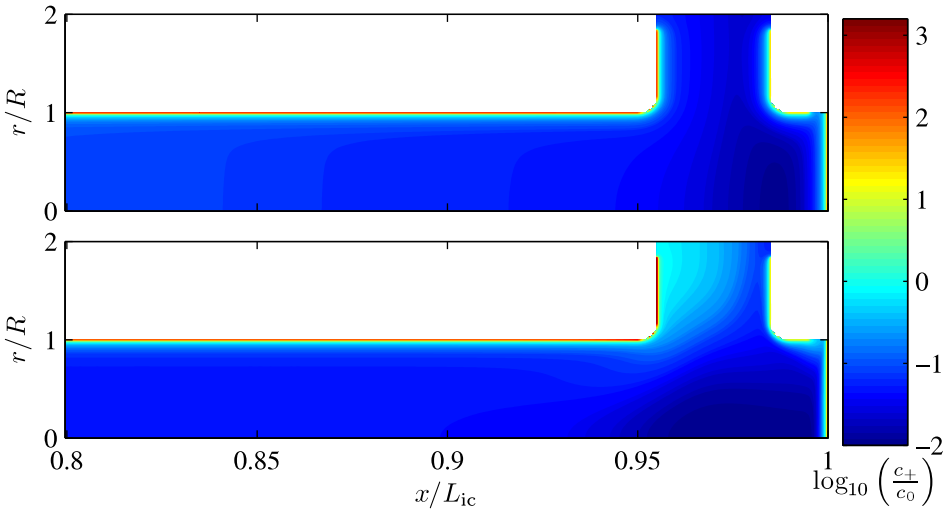

Figure 9.4: *Cation concentration in a desalination device for* $c_0 = 1\,\mathrm{mM}$ *and two bias voltages. Top: The cation concentration for the optimal bias voltage* $V_0 = 20V_\mathrm{T}$*. Bottom: The cation concentration for a bias voltage of* $V_0 = 300V_\mathrm{T}$*. The concentration in the side channel is seen to be considerably larger than in the inlet channel. Parameters:* pH = 7, $R = 0.6\,\mu\mathrm{m}$, $L_\mathrm{ic} = 20\,\mu\mathrm{m}$, $L_\mathrm{m} = 100\,\mu\mathrm{m}$, $L_\mathrm{oc} = 100\,\mu\mathrm{m}$, $L_\mathrm{out} = R$, $H_\mathrm{out} = R$.

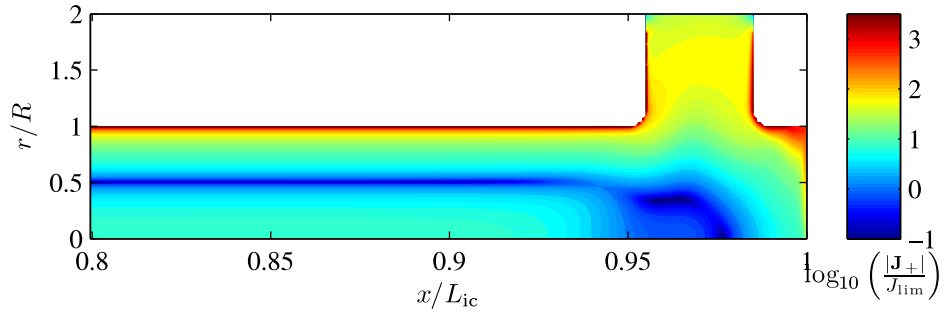

Figure 9.5: *Magnitude of the current density in a desalination device for* $c_0 = 1\,\mathrm{mM}$ *and* $V_0 = 300V_\mathrm{T}$*. The majority of the current is carried in the screening layers and in the side channel. Parameters:* pH = 7, $R = 0.6\,\mu\mathrm{m}$, $L_\mathrm{ic} = 20\,\mu\mathrm{m}$, $L_\mathrm{m} = 100\,\mu\mathrm{m}$, $L_\mathrm{oc} = 100\,\mu\mathrm{m}$, $L_\mathrm{out} = R$, $H_\mathrm{out} = R$.

through the side channels, because there will be plenty of surface conduction paths they can take. The minimum in figure 9.6 can thus be said to be an artifact of the modelling, and the physical system is expected to behave radically different from our model system.

Unfortunately there is no easy way to improve the modelling of the problem, since the existence of the alternate surface conduction paths is linked to the geometry. To include these paths we would have to make a full non-symmetric 3D model which would be extremely computationally demanding.

Given that our model system was able to desalinate water sufficiently, even though the lack of surface conduction paths should make it less efficient than the physical system,

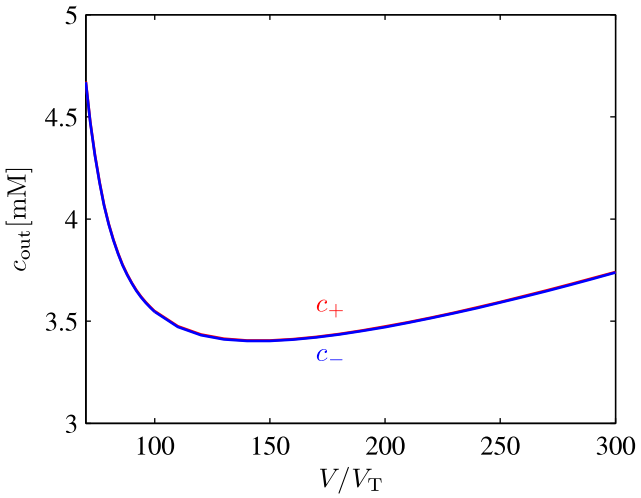

Figure 9.6: *Salt concentration at the side channel outlet for* $c_0 = 600\,\mathrm{mM}$ *(the cation and anion concentration curves overlap). There is seen to be a minimum for* $V_0 = 140V_{\mathrm{T}}$. *Parameters:* pH $= 7$, $R = 0.6\,\mu\mathrm{m}$, $L_{\mathrm{ic}} = 20\,\mu\mathrm{m}$, $L_{\mathrm{m}} = 100\,\mu\mathrm{m}$, $L_{\mathrm{oc}} = 100\,\mu\mathrm{m}$, $L_{\mathrm{out}} = R$, $H_{\mathrm{out}} = R$.

the system in figure 3.1 could be a viable design for a desalination device. As we cannot properly model the system, we can however neither predict the output of the system or at which efficiency it will run.

The considerations about the importance of different physical effects given in the start of the chapter are still expected to be valid.

Chapter 10

Conclusion and Outlook

In this thesis we have investigated a range of complex electrokinetic phenomena occurring in microchannels with ion-selective membranes. Starting from the simplest possible systems we have gradually increased the complexity of the relevant physics, and at each step rationalised the behaviour of the system. The simplest cases where investigated using an effective 1D model of the system which was developed for the purpose.

Comparing simulations with and without an included surface charge density we made the novel finding that the existence of a surface charge acts to decrease the amount of water ion generation in the system. This leads to a non-monotonic dependence of the current on the surface charge density, which is a counterintuitive result since the isolated effect of the surface charge is to increase the average conductivity.

To enable proper comparison between the I-V curves for constant surface charge density and the simple analytical result of Dydek *et al.* we extended the latter analysis to include the voltage drop over the membrane.

To investigate the effect of surface reactions on the surface charge density we included a simple local-equilibrium model of the reactions. The effect of this dynamic surface charge density on the system was the appearance of a second overlimiting regime, in which the differential conductance is decreased below the conductance in the initial overlimiting regime. In contrast the standard models assume the surface charge to be constant and as a consequence predict a constant differential conductance in the entire overlimiting regime.

To include the detailed effects of advection and to account for deviations from radial equilibrium some simulations of greater detail were carried out using an axisymmetric 3D model for the inlet channel. For large channel radii we found, as has previously been argued in the literature, that advection disturbs the depletion region enough to create a path for bulk conduction through the region.

In an attempt to combine the low computational cost of the 1D model and the accuracy of the axisymmetric 3D model, a model in which the 1D and 2D (axisymmetric 3D) models are coupled were developed. For narrow channels the model was found to be highly accurate, and using it an I-V curve for a comparatively long channel was found.

Finally, we constructed a simple model of a desalination device and simulated its op-

eration. Although some interesting findings were made it was ultimately deemed futile to continue the simulations as the model had some fundamental shortcomings. The physical realisation of the system we were trying to model has a complicated asymmetric structure, and in the course of our simulations we found this asymmetry, which we could not replicate in our axisymmetric model, to be of critical importance.

The results of this thesis point out several directions which could be pursued in future work.

Experimental verifications of the numerical results are of obvious interest. To enable direct comparison between experiments and numerical simulations a number of steps would be required. Firstly, a verification of the parameters in the dynamic surface charge model would be needed. This could be done by titration of a system including a frit of glass beads. Because the reservoir boundary conditions are difficult to realise for small systems the numerical model would also have to be extended to include dynamics at the electrodes.

Another interesting study would be to extend the numerical models to allow for modelling of the asymmetric desalination device. A full 3D model resolving the screening layers is probably too computationally demanding, but it is likely that a simplified model, in which the screening layers and the bulk are treated as separate regions which only couple through an effective boundary condition, could yield reasonable results.

Bibliography

[1] B. Albert, D. Bray, K. Hopkin, A. Johnson, J. Lewis, M. Raff, K. Roberts, and P. Walter, *Essential Cell Biology*. Garland Science, 2004.

[2] H. Bruus, *Theoretical Microfluidics*. Oxford University Press, 2008.

[3] M. Bazant and T. Squires, "Induced-charge electrokinetic phenomena: Theory and microfluidic applications," *Physical Review Letters*, vol. 92, pp. –, Feb. 2004.

[4] M. Bazant, M. Kilic, B. Storey, and A. Ajdari, "Towards an understanding of induced-charge electrokinetics at large applied voltages in concentrated solutions," *Advances in colloid and interface science*, vol. 152, no. 1-2, pp. 48–88, 2009.

[5] V. Nikonenko, N. Pismenskaya, E. Belova, P. Sistat, P. Huguet, G. Pourcelly, and C. Larchet, "Intensive current transfer in membrane systems: Modelling, mechanisms and application in electrodialysis," *Advances in colloid and interface science*, vol. 160, no. 1-2, pp. 101–123, 2010.

[6] W. H. Smyrl and J. Newman, "Double layer structure at the limiting current," *Transactions of the Faraday Society*, vol. 63, pp. 207–207, 1967.

[7] Y. I. Kharkats, "Theory of the exaltation effect and the effect of correlation exaltation of migration current," *Journal of Electroanalytical Chemistry and Interfacial Electrochemistry*, vol. 105, no. 1, pp. 97–114, 1979.

[8] M. B. Andersen, M. van Soestbergen, A. Mani, H. Bruus, P. M. Biesheuvel, and M. Z. Bazant, "Current-induced membrane discharge," *Arxiv preprint arXiv:1202.6448*, pp. –, 2012.

[9] E. Dydek, B. Zaltzman, I. Rubinstein, D. Deng, A. Mani, and M. Bazant, "Overlimiting current in a microchannel," *Physical Review Letters*, vol. 107, pp. –, Sept. 2011.

[10] S. H. Behrens and D. G. Grier, "The charge of glass and silica surfaces," *The Journal of Chemical Physics*, vol. 115, no. 14, pp. 6716–6716, 2001.

[11] I. Borukhov, D. Andelman, and H. Orland, "Steric effects in electrolytes: A modified Poisson-Boltzmann equation," *Physical review letters*, vol. 79, no. 3, pp. 435–438, 1997.

[12] M. Kilic, M. Bazant, and A. Ajdari, "Steric effects in the dynamics of electrolytes at large applied voltages. ii. modified Poisson-Nernst-Planck equations," *Physical Review E*, vol. 75, pp. –, Feb. 2007.

[13] M. Kilic, M. Bazant, and A. Ajdari, "Steric effects in the dynamics of electrolytes at large applied voltages. i. double-layer charging," *Physical Review E*, vol. 75, pp. –, Feb. 2007.

[14] C. E. Housecroft and E. C. Constable, *Chemistry*. Pearson Education Limited, 2006.

[15] A. G. Volkov, S. Paula, and D. W. Deamer, "Two mechanisms of permeation of small neutral molecules and hydrated ions across phospholipid bilayers," *Bioelectrochemistry and bioenergetics*, vol. 42, no. 2, pp. 153–160, 1997.

[16] C. Heitner-Wirguin, "Recent advances in perfluorinated ionomer membranes: structure, properties and applications," *Journal of Membrane Science*, vol. 120, no. 1, pp. 1–33, 1996.

[17] K. A. Mauritz and R. B. Moore, "State of understanding of nafion," *Chemical Reviews*, vol. 104, pp. 4535–4586, Oct. 2004.

[18] DuPont, *DuPont Nafion PFSA Membranes*, 2009.

[19] T. Xu, "Ion exchange membranes: State of their development and perspective," *Journal of membrane science*, vol. 263, no. 1, pp. 1–29, 2005.

[20] A. Elattar, A. Elmidaoui, N. Pismenskaia, C. Gavach, and G. Pourcelly, "Comparison of transport properties of monovalent anions through anion-exchange membranes," *Journal of membrane science*, vol. 143, no. 1, pp. 249–261, 1998.

[21] J. S. Mackie and P. Meares, "The sorption of electrolytes by a cation-exchange resin membrane," *Proceedings of the Royal Society of London*, vol. 232, pp. 485–498, 1955.

[22] Z. Lu, G. Polizos, D. D. Macdonald, and E. Manias, "State of water in perfluorosulfonic ionomer (nafion 117) proton exchange membranes," *Journal of The Electrochemical Society*, vol. 155, no. 2, pp. B163–B163, 2008.

[23] T. Hiemstra, W. Van Riemsdijk, and G. Bolt, "Multisite proton adsorption modeling at the solid/solution interface of (hydr)oxides: A new approach: I. model description and evaluation of intrinsic reaction constants," *Journal of Colloid and Interface Science*, vol. 133, pp. 91–104, Nov. 1989.

[24] R. K. Iler, *The Chemistry of Silica*. Wiley, 1979.

[25] P. W. Atkins, *Physical Chemistry*. Oxford University Press, 1994.

[26] L. H. Olesen, "Computational fluid dynamics in microfluidic systems," Master's thesis, Technical University of Denmark, 2003.

[27] COMSOL AB, *COMSOL Multiphysics Reference Guide*, 2011. Version 4.2.

[28] S. Brenner and L. R. Scott, *The Mathematical Theory of Finite Element Methods*. Springer, 1994.

[29] G. B. Arfken and H. J. Weber, *Mathematical Methods for Physicists*. Elsevier Academic Press, 2005.

[30] The Council of the European Union, "Council directive 98/83/ec: on the quality of water intended for human consumption." Official Journal of the European Communities, 1998.